Engineering Geology 355 (2025) 108233

Contents lists available at ScienceDirect

Engineering Geology

journal homepage: www.elsevier.com/locate/enggeo

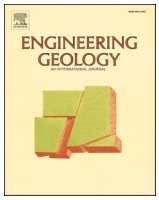

The delineation of graphite deposits of former mines in Lower Austria using the transient electromagnetic method

Jorge Luis Monsalve Martínez [a,*], Lukas Aigner [a], Philipp Högenauer [b], Adrián Flores Orozco [a]

[a] Research Unit of Geophysics, Department of Geodesy and Geoinformation, TU Wien, Vienna, Austria
[b] Geoelectrics and Radiometry, Department of Near Surface Geophysics, GeoSphere Austria, Vienna, Austria

ARTICLE INFO

Keywords:
Graphite exploration
Transient electromagnetic method
Geologic and geophysical interpretation
Polarization effects
Numerical modelling
Uncertainty analysis

ABSTRACT

Geological cross-sections (GCs) are valuable tools for understanding the subsurface, but their limitations become evident in the interpretation of deep mineral deposits, such as graphite. Typically, GCs are built based on near-surface observations and rely on the interpolation of the data; thus, also limiting the spatial resolution of the structures defined. Geophysical methods can play a crucial role in extending the interpretation of GCs both horizontally and vertically. This study investigates the effectiveness of the transient electromagnetic (TEM) method for graphite exploration in Lower Austria. We conducted TEM soundings to map large areas of difficult access and identify high electrical conductivity values (i.e., conductive anomalies) associated with potential graphite deposits. Our results demonstrate the strength of TEM as an efficient tool for graphite prospection, particularly suitable for abandoned mining areas and previously unexplored regions. We identified high-conductivity anomalies at depths of around 40 m, which correspond to surface areas where paragneiss and marble units are in contact, suggesting a high potential for flake-type graphite deposits. These anomalies align well with known graphite occurrences documented in geological maps. We also evaluate the abilities of the TEM method to map graphite-rich zones using numerical experiments.

1. Introduction

Graphite has been classified as a critical raw material by the European Commission due to its economic importance in the production of lithium-ion batteriesand the potential risk of supply disruptions (European Commission, 2020). This classification, along with the enactment of the Critical Raw Materials Act (European Parliament and Council of the EU, 2024), emphasizes the need for Europe to secure sustainable sources of critical materials, e.g., natural graphite, feldspar, manganese, nickel, etc.

Many Austrian graphite deposits have been mined in the past century. However, most graphite prospection and mining activities have focused only on shallow deposits, with large uncertainties regarding the graphite potential at a few tens of meters below the surface (Römer et al., 2021, 2022). The high demand for graphite, for instance, for sustainable production and storage of energy, has prompted the interest in exploring and exploiting abandoned mines as well as investigating for potential deeper deposits. This has driven the development of innovative exploration techniques, including semi-airborne geophysical methods utilizing unmanned aerial vehicles (UAVs), as demonstrated by Mörbe et al. (2024).

Geological cross-sections (GCs) are a fundamental approach for understanding the spatial distribution of lithologies, structures and geological relationships at specific depths and directions. However, the creation of GCs often relies on surface observations or occasional boreholes (Ragan, 2009; Fossen, 2010; Martín et al., 2013). This reliance can lead to crude interpolations or assumptions based on limited information, potentially resulting in misleading interpretations, particularly concerning the geometry of deep structures. Geophysical methods can overcome this challenge by producing quasi-continuous models of physical properties through data inversion (Binley et al., 2015), enhancing the interpretation of GCs both laterally and vertically (e.g., Hatherly, 2013; Binley et al., 2015; Sandersen et al., 2021). Therefore, integrating GCs with geophysical data is essential for a thorough understanding of subsurface structures (e.g., Galdón et al., 2017), facilitating the quantitative interpretation of geophysical results, such as estimating graphite content (Katona et al., 2024).

Graphite behaves as an electrical conductor, allowing electrons to move freely in the presence of an external electrical field, which results in high electrical conductivity (e.g., Gautneb et al., 2020b; Sakita et al.,

* Corresponding author.
E-mail address: jorge.martinez@geo.tuwien.ac.at (J.L. Monsalve Martínez).

https://doi.org/10.1016/j.enggeo.2025.108233
Received 13 September 2024; Received in revised form 11 April 2025; Accepted 5 July 2025
Available online 7 July 2025

2022; Gautneb et al., 2023; Katona et al., 2024). This mobility of free electrons also leads to the polarization of charges when exposed to an external electrical field, which can be measured by means of the induced polarization (IP) method, as initially reported by Olhoeft (1985). As a non-metallic electronic conductor, graphite is expected to exhibit strong polarization responses, as confirmed by laboratory IP experiments conducted at low frequencies. Katona et al. (2024) performed Spectral Induced Polarization (SIP) measurements at both the laboratory and the field scale to identify graphite content. Their results indicate that zones with high conductivity values ($>$ 150 mS/m in the field and $>$ 500 mS/m in laboratory plug samples) and high polarization values ($>$ 0.1 rad in the field and $>$ 0.3 rad in laboratory plug samples) are associated with graphite-rich rocks. Additionally, Revil et al. (2015, 2017) and Wu and Peruzzo (2020) have reported polarization magnitudes, with phase shifts exceeding 0.2 rad. These strong polarization effects are associated to the so-called electrode polarization mechanism (Wong, 1979), which has been further developed by Revil et al. (2015) and Bücker et al. (2018, 2019). Consequently, there is a growing interest in applying electrical and electromagnetic methods, sensitive to IP response, for graphite prospection at the field-scale (e.g., Marescot et al., 2008; Revil et al., 2015, 2017; Wu and Peruzzo, 2020; Revil et al., 2022; Katona et al., 2024).

The IP method is a well-established electrical geophysical technique in raw material prospection (e.g., Seigel et al., 1997). It is the extension of traditional direct current (DC-resistivity) methods, as it provides both electrical conductivity and capacitive properties (e.g., Wong, 1979). IP measurements can be used to quantify metallic content as well as the textural properties (i.e., grain sizes) of the mineral ore (e.g., Pelton et al., 1978; Wu and Peruzzo, 2020; Revil et al., 2017; Katona et al., 2024). However, IP measurements require extensive cabling and galvanic contact between the ground and the electrodes used to conduct the measurements, making the exploration of large areas logistically challenging and potentially inefficient for graphite exploration. Electromagnetic methods can overcome these limitations, as these are carried out with contactless instruments, allowing to reduce time for the investigation of large areas. In particular, the transient electromagnetic (TEM) method has become a well-established technique for near-surface investigations, offering flexibility to reach varying depths using different measurement configurations (e.g., Christiansen et al., 2006). Moreover, new instruments enable the collection of continuous datasets with equipment towed by vehicles (e.g., Harris et al., 2006; Auken et al., 2019; Sandersen et al., 2021), boats (e.g., Lane Jr et al., 2020; Yogeshwar et al., 2020; Aigner et al., 2021; Bücker et al., 2021) and UAVs (e.g., Mogi et al., 2009; Wu et al., 2019; Mörbe et al., 2024), demonstrating the capability to easily cover geological scales.

In this study, we employ the TEM method to investigate areas surrounding former graphite mines in Lower Austria (ca. 1730 ha). Due to the absence of boreholes, geological assessments have been limited to the analysis of outcrops and surface samples. Our primary objective is to identify graphite-rich zones at depths between 10 and 70 m. This study follows a four-stage approach. In the first stage, we present a GC constructed from limited surface geological information. In the second stage, we validate our data and inversion results by conducting numerical experiments to demonstrate that the device used in this study can effectively measure high conductivity contrasts and to investigate the effects of polarization in the inversion process. In the third stage, we delineate graphite deposits by inverting TEM data, generating a GC based on geophysical interpretations, and refining the location of a fault using high conductivity contrasts. In the fourth stage, we evaluate the performance and accuracy of our methodology by comparing the results with those independently obtained using a transdimensional Markov chain Monte Carlo (MCMC) algorithm, also known as reversible jump MCMC (Green, 1995). Specifically, we utilized the TransdEM software package developed by Peng et al. (2022) for transdimensional Bayesian inversion of electromagnetic (EM) data in horizontally stratified resistivity media.

2. Materials and methods

2.1. Geology settings and graphite deposits in Lower Austria

Austria possesses graphite occurrences in four provinces (Gautneb et al., 2020a). The northwestern Moldanubikum (Bavarikum) province boasts historical production until 1963, with the Veitsch Nappe hosting Austria's sole active mine at Kaisersberg (420 tons/year). Further south, the Drau-Mur area of Styria saw periodic mining activity up to 1916 (Ucik, 1992; Schuster et al., 2006). Finally, the northeastern Dosendorf province, characterized by Proterozoic rocks, witnessed graphite mining at around 30 sites between 1895 and 1994 (Hofbauer, 1995).

The Hengstberg graphite deposits lie in Lower-Austria, on a ridge (Dachertberg, 442 m) south of the village of Hengstberg. Geologically, the deposit belongs to the Drosendorf Nappe System ("Bunte Serie") within the Moldanubian zone. This zone is characterized by graphite-bearing marble and paragneiss (Römer, 2024; see Fig. 1).

According to Gautneb et al. (2020a), there are four categories of organic matter classified by their crystallographic order, with natural char being the least ordered and graphite being the most. Graphite deposits typically form when organic material is metamorphosed, releasing volatile compounds like CO_2, CH_4, and H_2O during the early stages (Gautneb et al., 2020a). The size and type of starting material, along with the pressure and temperature conditions, influence the resulting graphite. There are two main categories: microcrystalline (amorphous) graphite with grains smaller than 75 μm, and macrocrystalline (flake) graphite with larger grains (Damm, 2021). Flake graphite, formed at temperatures exceeding 650 °C, is the most industrially relevant type due to its use in lithium-ion battery anode production (Tian et al., 2024).

The Hengstberg area boasts flake graphite deposits with potential economic value. Historical mining activity occurred around 1905 and 1921–1930, with a documented 500 m gallery (Weber et al., 2019). However, the mine has been abandoned due to the low graphite production from near-surface. The lack of deep drillings has limited the investigations of the site; nonetheless, it is critical to evaluate the graphite potential in the area at non-explored depths.

2.2. Geological cross-section as a first approach

The study area is located at the junction of the southern part of the Mautern sheet (map 37) and the northern part of the Upper Grafendorf sheet (map 55) of the Geological Map of Austria (Fig. 1). These maps, published by GeoSphere Austria at a scale of 1:50.000, were produced in 1983 and 2012, respectively. Based on this information, we built the GC A-A', which is approximately 4 km long and located in the south-central portion of the Mautern sheet (map 37). Its initial orientation is S85°W – N85°E for the first 2.5 km, followed by a change to S72°W – N72°E. This orientation prioritizes understanding the presence of graphite in areas with known graphite-bearing rocks or historical graphite mines. Due to the inconsistencies in geological interpretation of those maps, the B-B' cross-section based on map observations is not presented in this study, as it would intersect features from both maps (Fig. 1). Accordingly, the

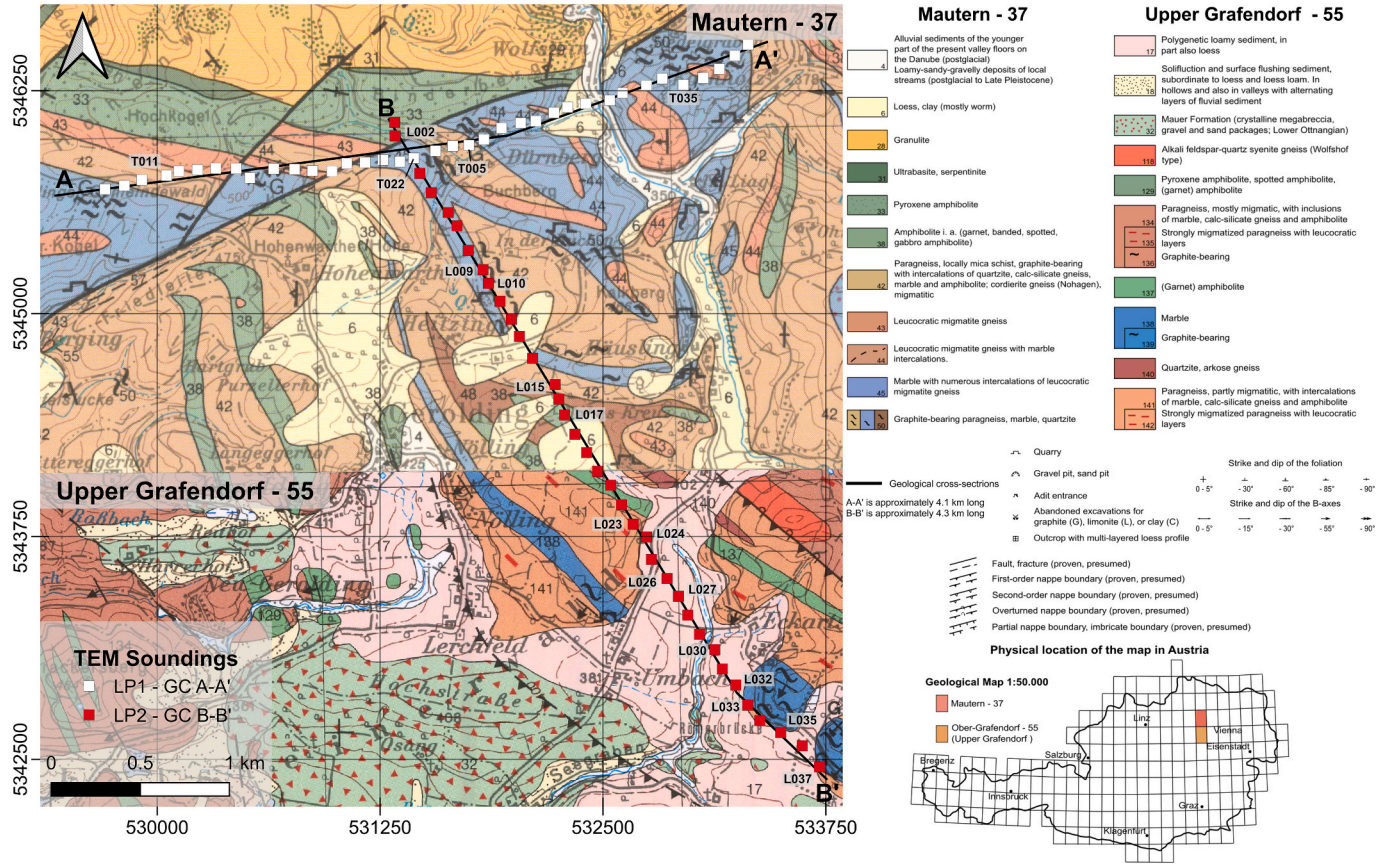

Fig. 1. Geological map of the study area, integrating the southern portion of the Mautern map (37) published in 1983 and the northern portion of the Upper Grafendorf map (55) published in 2012. Both portions represent geological information at a 1:50,000 scale. The black lines indicate the geological cross-sections (GCs) analyzed in this study: A-A', oriented SW to NE in the northern part of the area, and B-B', oriented NW to SE in the central part of the study area. White and red squares represent the TEM soundings (25 m loop size) used to construct profiles LP1 and LP2 along GC A-A' and B-B', respectively. T: Transversal, L: Longitudinal. The intersection of both profiles is located at sounding T022. (For interpretation of the references to colour in this figure legend, the reader is referred to the web version of this article.)

construction of the cross-section B-B' is one of the results of the geophysical investigation presented here. This B-B' cross-section is situated around the middle of the study area, its initial orientation is N32°W – S32°E for the first 3.78 km, followed by a change to N47°W – S47°E, and is also approximately 4 km long (Fig. 1). The structural bearing (β angle) in the A-A' cross-section varies from 40° to 55°, and in the B-B' cross-section, it ranges from −8° to −23°, creating an oblique orientation in both cross-sections. In these cases, due to the obliqueness of the cross-sections, as mentioned by Ragan (2009) and Fossen (2010), plotting the true dip (δ; steepest line on a plane measured perpendicular to the structural strike, S) of the structural data is not possible and is commonly referred to as apparent dip (α; inclination of an oblique line on a plane). To correct this, the analytical solution $\tan\alpha = \tan\delta\sin\beta$ is used, which is based on the trigonometric equation proposed by Herold (1933), where β is the result of subtracting the angle of the line representing the GC (compass bearing (θ)) from S.

The available structural information in the study area was not sufficient to establish a value for all the contacts intersected with the GC presented in Fig. 2. According to Gerald Schubert-Hlavac (personal communication, December 2023), the Schönbühel-Gerolding area (Fig. 1) is characterized by lithological features being mainly oriented with a dip direction of 215/37. Lithological boundaries with irregular features (e.g., discordant intrusive igneous bodies) were projected at shallow depths as a first approximation using the same value; deeper interpretations depend on the expert's prior knowledge (Ragan, 2009; Fossen, 2010).

2.3. Transient electromagnetic method

TEM soundings were acquired in October 2023 and February 2024 in the vicinity of former graphite mines in Lower Austria. The investigation targeted graphite deposits using two long profiles aligned with the previously described GCs (A-A' as profile 1 and B-B' as profile 2). Each profile spans approximately 4 km and comprises 37 TEM soundings, spaced about 110 m apart, as shown in Fig. 1. We used the TEM-FAST 48 device, manufactured by AEMR (Applied Electromagnetic Research, Utrecht, the Netherlands), in the single-loop configuration. For each sounding, a 25 m loop size was employed, with the excitation based on a current of 4 Amperes imposed in the transmitting loop at a voltage of 24 V. The voltage decay was measured in 36 active windows, covering a time range from 4 μs to 1900 μs, with a stacking of 4680 pulses.

We visualize all soundings to evaluate data quality and identify outliers and erroneous soundings. By evaluating decay curves, we determined the need for filtering specific windows due to contamination

Table 1
Overview of the TEM profiles, corresponding soundings, and the filtering and inversion parameters applied. Columns 1 and 2 list the profiles and associated TEM soundings, while Columns 3 and 4 specify the initial and final time ranges (respectively) considered for each sounding. Column 5 presents the inversion parameters used in the study.

Profile	TEM sounding	t_{min} (μs)	t_{max} (μs)	Inversion parameters
	T033		40	
	T007, T037		50	Number of layers
	T012		60	6
1	T013		90	Lambda (λ)
A - A'	T010, T016, T032, T034	8	100	[500]
4.1 km	T004, T009, T011, T035		200	Cooling factor
SW - NE	T002		300	[0.8]
	T017, T020, T021, T031		500	Noise floors (%)
	T026		700	(1, 3, 5, 7)
	T001, T003, T005, T006, T014, T015, T019, T022, T023, T024, T025, T027, T028, T029, T008, T030, T036		1000	
	L013		50	
	L019		90	
	L018, L020		100	Number of layers
	L017		150	6
2	L016, L021, L023		200	Lambda (λ)
B - B'	L006, L014, L015, L024	8	300	[500]
4.3 km	L022		400	Cooling factor
NW - SE	L002		600	[0.8]
	L012, L025		700	Noise floors (%)
	L032, L033		800	(1, 3, 5, 7)
	L026, L027		900	
	L004, L005, L007, L008, L009, L010, L011, T022, L028, L029, L030, L031, L034, L035, L036, L037		1000	

from the turn-off ramp or low signal-to-noise ratio (S/N), both of which are influenced by the loop size. A larger loop increases the length of the turn-off ramp, primarily affecting the early-time voltage readings, while late-time measurements are more affected by the reduced S/N (e.g., Raiche, 1984; Fitterman and Anderson, 1987; Zeng et al., 2019; Aigner et al., 2021, 2024). For the 74 soundings, the initial time range selected was 8 μs. The final time range varied from 100 μs to 1000 μs depending on the smoothness and quality of each sounding, as shown in Table 1. This table also lists the inversion parameters, including the number of layers, regularization criterion (λ), cooling factor, and noise floors. Different noise floor values were tested to assess their influence on the inversion results, with 7 % selected based on the lowest relative root-mean-square error (rRMSE).

For the forward modelling and inversion of the TEM data, we employed the code developed by Aigner et al. (2024), specially designed for the TEM-FAST 48 instrument. This code performs real-valued 1D inversions to resolve variations in electrical conductivity at depth, defined by a finite number of layers. Additionally, it can model polarization effects in TEM data by resolving the frequency dependence of complex conductivity for each layer. To achieve this, the forward modeler uses the maximum phase angle (MPA) model proposed by Fiandaca et al. (2018), which calculates the frequency dependence of electrical properties while minimizing the correlation between the chargeability and the dispersion coefficient, thereby stabilizing the inversion of TEM data with polarization effects. The algorithm quantifies data fit using both the rRMSE and the weighted root-mean-square error (χ^2). It also estimates the depth of investigation (DOI) to which the inverted model is sensitive, using the classical skin-depth approach by Spies (1989), which can be calculated following the method outlined by Yogeshwar et al. (2020). The DOI has been used in previous studies to estimate the maximum depth at which TEM inversion results remain constrained by the data (e.g., Yogeshwar et al., 2020; Bücker et al., 2021; Aigner et al., 2024). For more detailed information on the equations underlying the forward modelling and the inversion methodology, refer to Aigner et al. (2024).

In the following chapter, we present the TEM inversion results and their interpretation as GCs. However, the lack of ground truth limits a quantitative evaluation of the results. To address this, we assess the uncertainty by comparing our inversion outcomes using the code developed by Aigner et al. (2024) and the Julia-based TransdEM software package by Peng et al. (2022), implemented in the Julia programming language (Bezanson et al., 2017). TransdEM operates within a Bayesian inference framework, where the solution to the inverse problem is expressed as a posterior probability distribution (PPD) of model parameters (e.g., number of layers, layer thicknesses, and interface depths), providing insights into parameter uncertainties (Mosegaard and Tarantola, 1995; Sambridge and Mosegaard, 2002; Kaipio et al., 2000). Bayesian inference aims to approximate the target PPD using a large ensemble of feasible models generated through an appropriate sampling algorithm. The most widely used approach is MCMC (Green, 1995), which has proven effective for EM data inversion (e.g., Blatter et al., 2018; Killingbeck et al., 2020; Peng et al., 2022). This approach combines Monte Carlo simulations with Markov chain techniques and improves uncertainty estimation without requiring a fixed number of model parameters (Agostinetti and Malinverno, 2010; Ray et al., 2014). In this process, Monte Carlo sampling randomly perturbs model parameters, while the Markov chain guides the selection of accepted models. For further details on the theoretical foundations, implementation, and versatility of TransdEM, see Peng et al. (2022).

3. Results and discussion

3.1. Geological cross-section A-A'

Fig. 2 shows GC A-A', constructed using the available geological data. The dip of the rocks along GC A-A' was calculated using the trigonometric equation proposed by Herold (1933), resulting in a dip of 215/26 for the first portion (0–2.5 km profile distance) and 215/32 for the second portion (beyond 2.5 km). This GC intersects two faults, which, based on surface geological map analysis, are interpreted as dextral strike-slip faults. However, the lack of kinematic indicators such as slickensides prevents the confirmation of the exact sense of shear

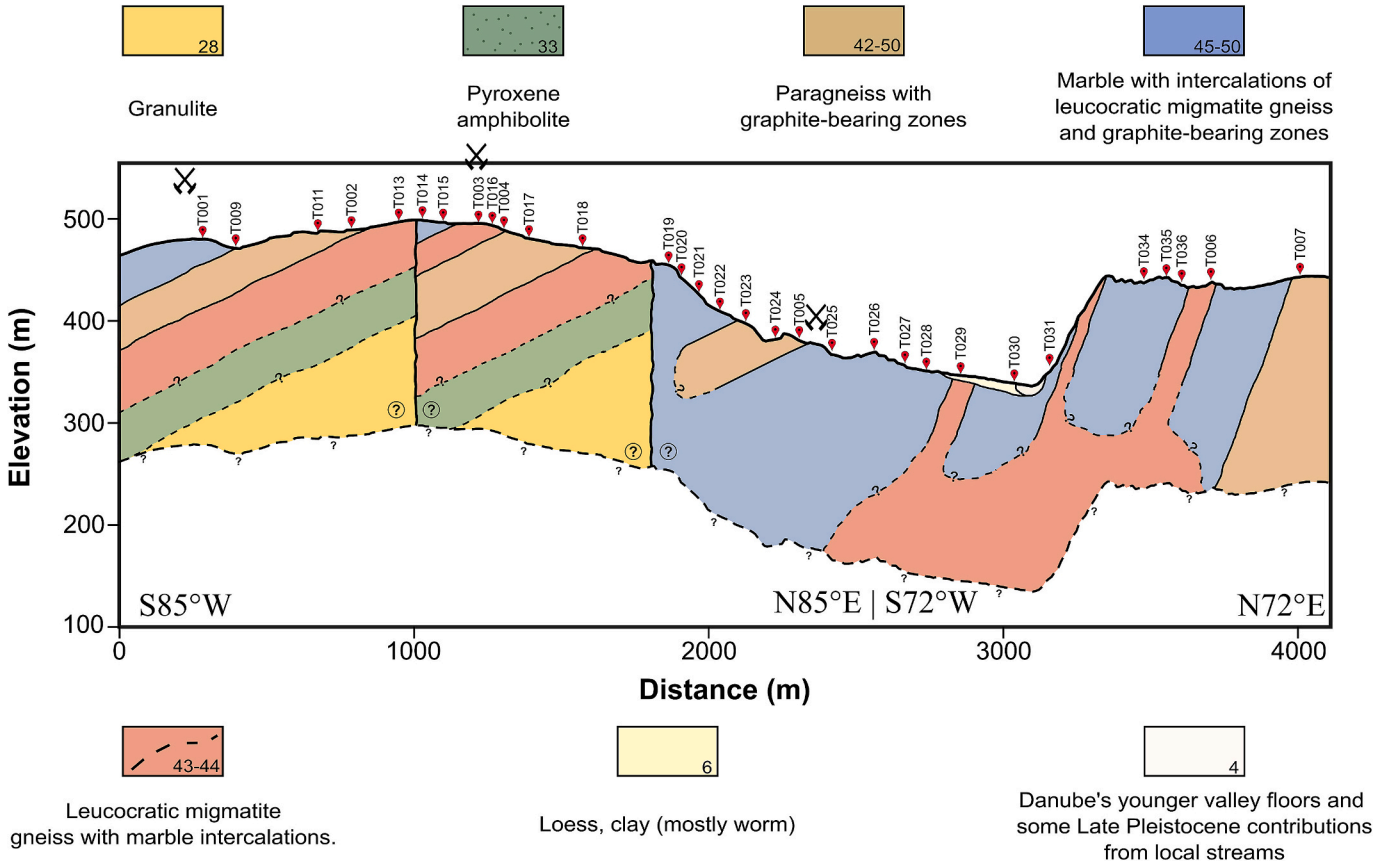

Fig. 2. GC A-A', constructed using surface geological data to depict the distribution of different rock units intersected. The sense of shear on the fault surfaces is unknown (represented by circled question marks). Deeper rock units are interpreted by the authors (dashed lines with question marks in the GC A-A') due to the absence of direct subsurface data (e.g., wells), which are necessary for validation. The three black symbols at approximately 250 m, 1250 m, and 2400 m along the profile mark the locations of former graphite mines. Red symbols and black text denote the positions and names of the TEM soundings, respectively. (For interpretation of the references to colour in this figure legend, the reader is referred to the web version of this article.)

along these fault surfaces, as indicated in Fig. 2.

The GC A-A' indicates crystalline basement rocks overlain by younger sedimentary rocks (Fig. 2). The crystalline basement consists of leucocratic migmatite gneiss with marble intercalations (units 43 and 44), marble with abundant leucocratic migmatite gneiss and zones containing graphite (units 45 and 50), and paragneiss that also includes graphite-bearing zones (units 42 and 50). The younger rocks include alluvial sediments deposited on the younger portions of the present Danube valley floor (postglacial), loamy-sandy-gravelly deposits left behind by local streams (deposited from the postglacial period to the Late Pleistocene; unit 4), and loess (unit 6). Our geological contacts presented at depth are based on our interpretation of the geological maps available and will be further evaluated using geophysical data. In this regard, Fig. 2 highlights that the lack of direct geological information complicates the delineation of graphite-rich areas, and thus, the necessity to include geophysical data for an adequate interpretation of deep geological contacts.

3.2. TEM soundings: evaluating the ability to identify and interpret graphite rich-areas

Fig. 3 shows raw data and inversion results for soundings L035 and, L030 and L017. The soundings L035 and L030 were in areas where graphite is expected; whereas sounding L017 was conducted in a location where no graphite is expected. The decay curve for the sounding L035 (Fig. 3a) spans four orders of magnitude (10^{-3} V/m^2–10^{-7} V/m^2) and exhibits a smooth decay, associated to apparent conductivity (σ_a) values that range between 50 mS/m and 200 mS/m (Fig. 3b). The inversion result for this sounding is characterized by a 3-layers model (Fig. 3c). The first layer, with a thickness of 20 m, has a conductivity (σ) of ca. 70 mS/m, which is associated with polygenetic loamy sediments, which can be in part also loess (unit 17; c.f., Fig. 1). The intermediate layer, with a thickness of approximately 65 m, shows the highest σ values (120 mS/m to 300 mS/m), which are related to the transition between partly to strongly migmatized paragneiss that include intercalations of marble and leucocratic layers (units 141 and 142; c.f., Fig. 1), and graphite-bearing marble (units 138 and 139; c.f., Fig. 1), which indicates the presence of graphite. The third (and bottom) layer shows a decrease in electrical conductivity (ca. 80 mS/m), suggesting lower graphite content than the second layer, and is likely related to migmatized paragneiss that include intercalations of marble (141 and 142; c.f., Fig. 1).

The decay curve measured at sounding position L030 (Fig. 3d) extends over five orders of magnitude (10^{-3} V/m^2–10^{-8} V/m^2). The σ_a curve (Fig. 3e) has lower values ranges compared to L035 (Fig. 3b), varying from 15 mS/m to 70 mS/m. The inversion results for L030 (Fig. 3f) are comparable to those for sounding L035, but with some differences: the first layer exhibits lower conductivity (approximately 18 mS/m) and larger thickness (around 33 m). The second layer, ca. 53 m thick, displays σ values between 85 mS/m and 150 mS/m, lower than those observed in L035, suggesting the presence of graphite-rich rocks but in lesser quantities. The third layer, extending beyond ca. 85 m, shows intermediate σ values (ca. 50 mS/m); similar to those of the third layer of L035. These layers can be related to the transition of marble (units 138 and 139; c.f., Fig. 1), partly to strongly migmatized graphite-bearing paragneiss that include intercalations of marble and leucocratic

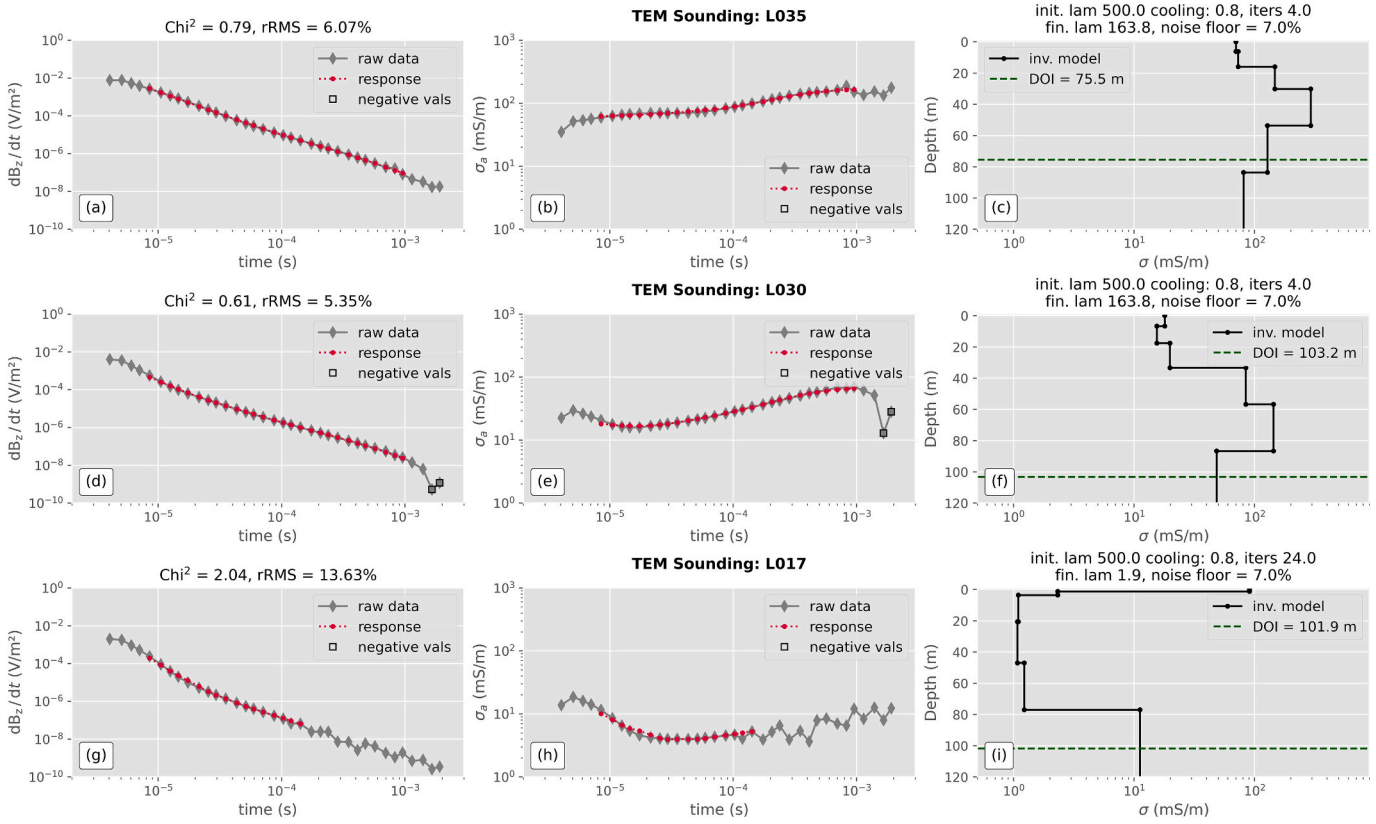

Fig. 3. Three representative TEM soundings and their inversion results. Data fit (a), apparent conductivity (b), and inversion result (c) for sounding position L035, located at a former graphite mine. Data fit (d), apparent conductivity (e), and inversion result (f) for sounding position L030, located 600 m northwest of L035. Data fit (g), apparent conductivity (h), and inversion result (i) for sounding position L017, where no graphite is expected in the subsurface.

layers (units 141 and 142; c.f., Fig. 1), and weathered quartzite-arkose gneiss (unit 140; c.f., Fig. 1), respectively.

The TEM decay curve at position L017 (Fig. 3g) shows a range of six orders of magnitude (10^{-3} V/m^2–10^{-9} V/m^2). At ca. 120 μs, the quality of the decay curve deteriorates, indicating a poor signal-to-noise ratio (S/N). Fig. 3h shows that L017 position is characterized by the lowest σ_a ranges (3 mS/m to 10 mS/m) compared to L035 (Fig. 3b) and L030 (Fig. 3e). A 2-layers model distinguishes the inversion result (Fig. 3i), which exhibits lower σ values compared to the previous soundings, confirming the lack of electrical conductors, i.e., graphite. The first layer has a thickness of ca. 75 m and an electrical conductivity of ca. 1 mS/m and is associated to metamorphic rocks without graphite content (e.g., quartzite-arkose gneiss – unit 140; c.f., Fig. 1). The second layer, situated at a depth of ca. 75 m, exhibits an increased σ of ca. 100 mS/m, associated with the transition to migmatized graphite-bearing paragneiss that include intercalations of marble and leucocratic layers (units 141 and 142; c.f., Fig. 1). In this case, the low conductivity of the first layer and the underlying conductive material contribute to a lower impulse response detected by the receiving antenna. Consequently, the observed fluctuations in the late-time data (Fig. 3g) are not attributed to noise sources but to a low S/N ratio resulting from the absence of conductive material.

In Fig. 3c, f, and i, the corresponding DOI for each sounding is shown. Sounding L017, which shows a transition from a resistive to a conductive layer at depth, exhibits a larger DOI than soundings L035 or L030, which transition from conductive to resistive layers (see Fig. 3b, e, and h). The presence of highly conductive materials enhances the propagation of EM fields and increases signal strength (see Aigner et al., 2021). Hence, a deeper conductive layer improves the DOI, while a deep resistive layer results in a shallower DOI, as the current is primarily confined to the shallow conductive zones (Christiansen et al., 2006; Nagendran, 2024).

Inversions of the TEM data revealed six soundings from each profile with a high rRMSE (> 30 %), making them unsuitable for further analysis and will not be presented here. We conducted numerical experiments to evaluate the precision of our measurements in resolving vertical conductivity variations associated with the resistive host rocks and the conductive graphite structures. These experiments were further validated by comparing the numerical results with real field data from three representative soundings. The experiments involved two three-layer models, each with a 10 m thick first layer, having conductivity values of 20 mS/m and 2 mS/m, respectively (Fig. 4). The remaining two layers were consistent in both models, with the second layer being 50 m thick and having a conductivity of 100 mS/m. The third layer, also 50 m thick, had varying conductivity values of ca. 3 mS/m, 12.5 mS/m, and 33 mS/m, resulting in six distinct scenarios. To achieve an acceptable fit in the 1D inversion, we selected a relatively low regularization parameter ($\lambda = 10$) and applied a relative error floor of 3 %. Additionally, we varied the number of layers for the model response (3, 6, and 30 layers), as well as the initial conductivity values, using the mean value of the apparent conductivity (σ_a), ten times the mean value of σ_a, and values of 3.3, 10, and 33.3 mS/m.

Our numerical experiments reveal that the inversion accurately retrieves the conductivity of the top layer when the contrast in electrical conductivity between adjacent layers is low (Fig. 4a to c), compared to cases with a high contrast (Fig. 4d to f). This can be attributed to the smoothness constraint imposed by our algorithm, which hinders the resolution of sharp conductivity contrasts. A similar effect is observed in the third layer. Despite minor discrepancies between the synthetic data and model response, the strong contrast between conductive and resistive layers remains well-resolved, regardless of the initial model used for the inversion. These numerical experiments are crucial for identifying

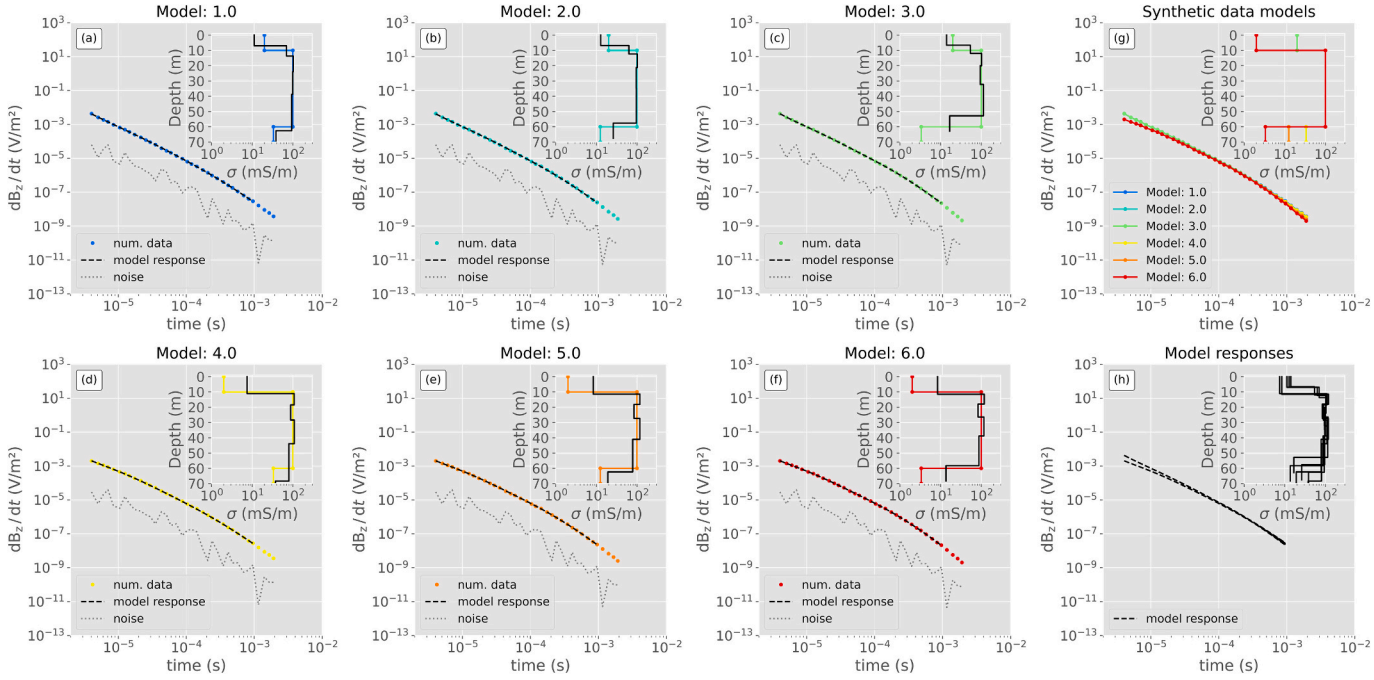

Fig. 4. Numerical experiments modelling a 50 m conductive layer interbedded between two resistive layers with varying conductivity values. The first layer is 10 m thick, with conductivity values of 20 mS/m and 2 mS/m. The second layer is 50 m thick with a conductivity of 100 mS/m. The third layer, also 50 m thick, has varying conductivity values of approximately 3 mS/m, 12.5 mS/m, and 33 mS/m. Changing the conductivity of the first and third layers results in six distinct scenarios (a-f). A summary of the different models and their inversion responses is provided in (g) and (h), respectively.

potential graphite-rich zones, as they highlight the significant contrast between the high electrical conductivity of the target material (i.e., graphite) and the high electrical resistivity of the surrounding host material.

Results from the numerical experiments presented in Fig. 4 indicate that, while a three-layer model can fit the data, its use of thick layers risks oversimplifying the subsurface and misrepresenting the boundaries of graphite-rich areas. In contrast, employing a model with a larger number of layers may improve vertical resolution but introduces the risk of artefacts – layers that fit the data but do not accurately represent the geological medium. This non-uniqueness is a well-known issue in the inversion of geophysical data (e.g., Ellis, 1998; Zhdanov, 2002; Binley et al., 2015; Puzyrev, 2019), where multiple models can explain the same measurements. Therefore, inversion must be conducted with appropriate settings and analyzed through both numerical modelling and geological data to provide a reliable interpretation. In our case, the absence of borehole data limits our evaluation to geological maps and surface data. Given the simple geology of the area, we opted for simpler models with fewer layers (6) to identify potential graphite units at depth. Our evaluation revealed that defining the initial model with values such as ten times the mean value of σ_a, or using fixed values of 3.3 mS/m and 10 mS/m, resulted in either underfitting or overfitting of the conductive middle layer, with overfitting being most pronounced at 33.3 mS/m. The six-layer inverted model (Fig. 4h), which used the mean value of σ_a as the initial conductivity model (Fig. 4g), achieved a good fit, resolving the high contrast between the conductive material associated with graphite-rich zones and the surrounding high-resistivity rocks. Consistent settings for filtering and inversion across all soundings aimed to ensure comparable inversion results.

3.3. Considering polarization effects in TEM data for graphite quantification

Recent studies emphasize the importance of accounting for polarization effects in the modelling and inversion of TEM data, which is crucial for quantitatively interpreting electrical properties in relation to ore exploration (Flores and Peralta-Ortega, 2009; Yu et al., 2013; Zeng et al., 2019; Kang et al., 2020; Maurya et al., 2022; Aigner et al., 2024). As discussed above, high conductivity values can reliably indicate the presence of graphite; thus, we argue that real-valued inversion of TEM data remains effective for geological investigations and for assessing the geometry of graphite-bearing formations at a geological scale. In the following, we evaluate the impact on this interpretation in case that the inversion of the TEM data considers complex conductivity and its frequency dependence.

Fig. 5 presents the results of numerical simulations comparing the effects of including and excluding polarization effects in the inversion of a six-layer model for soundings T005 and T011. Sounding T005 reveals a polarizable unit within conductive media, indicative of graphite presence (Fig. 5a to c), while sounding T011, associated with resistive non-polarizing media, corresponds to metamorphic rocks lacking graphite content (Fig. 5d to f). For the graphite-rich sounding (T005), the first layer (ca. 6 m thick) displays intermediate conductivity (ca. 30 mS/m, see Fig. 5a). The inversion results for this layer remain consistent regardless of whether polarization effects are considered (Fig. 5a and b). The second layer (ca. 6 m to ca. 20 m depth) also reveals consistent values (ca. 10 mS/m) in both inversion approaches (Fig. 5a and b). When polarization is considered (Fig. 5b), the conductivity of the third layer (ca. 20 - ca. 38 m depth) increases by 50 %, reaching ca. 20 mS/m, with both the second and third layers exhibiting low but non-negligible polarization values (ca. 0.1 rad; Fig. 5c). The fourth, fifth, and sixth layers likely correspond to the same graphite-bearing unit (extending from ca. 38 m to the bottom) and are characterized by the highest conductivity values (up to 180 mS/m) as well as by strong polarization values (ϕ_m values from 0.4 to 0.5; Fig. 5c). Inversions considering polarization effects fail to retrieve the expected conductivity values for deep layers. This discrepancy is due to the non-uniqueness in the inversion where different models can explain the data. Hence including

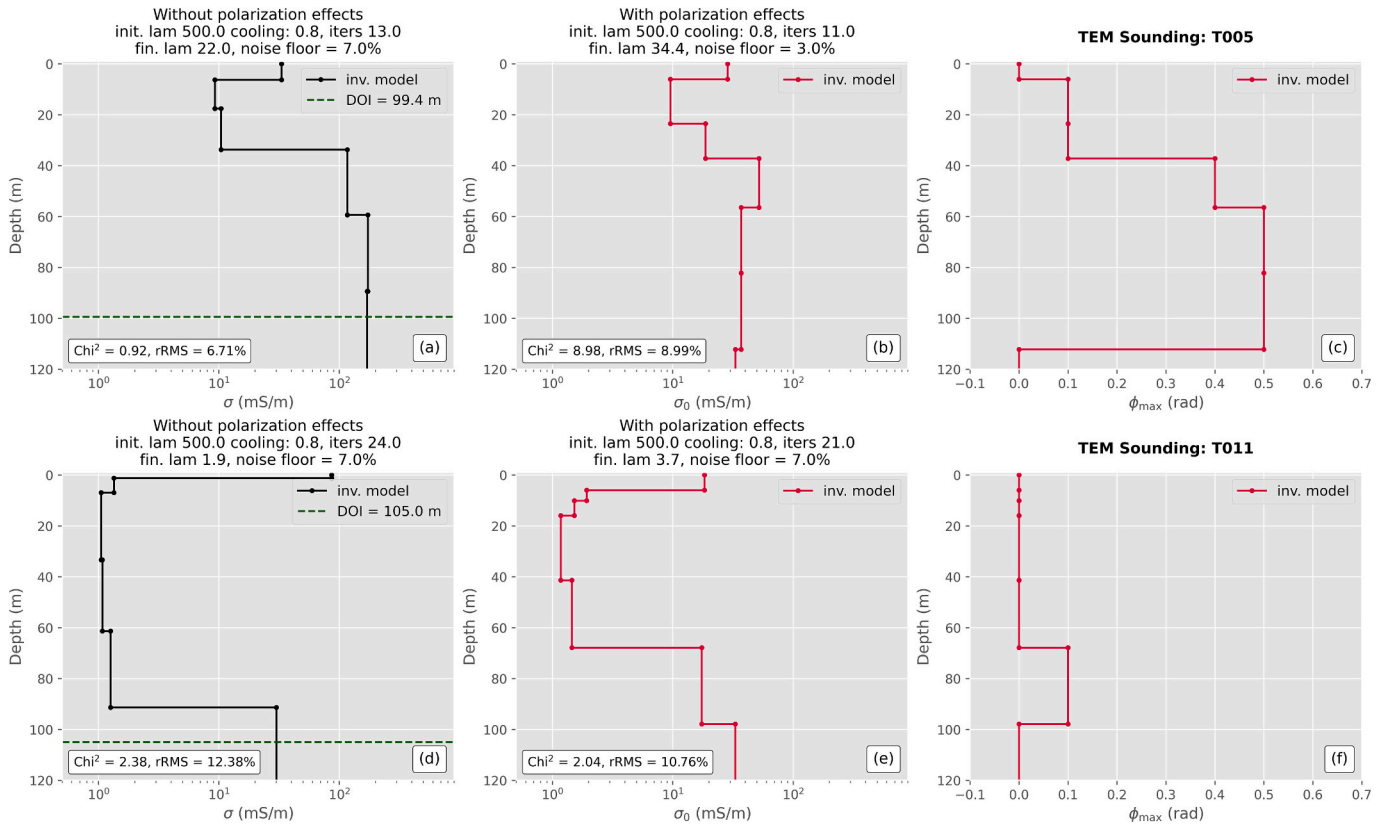

Fig. 5. Comparison of TEM inversion results for two sounding positions from profile LP1 without (a and d) and with polarization effects (b-c and e-f). Sounding position T005 (a-c) corresponds to a former graphite mine, and sounding position T011 (d-f) corresponds to a location where no significant graphite content is expected in the subsurface.

further model parameters to describe the frequency dependency of the complex resistivity, increases the instability in the inversion (see Aigner et al., 2024 for a detailed discussion). Further research involving deeper investigations, for instances acquiring measurements at later times and higher magnetic moments, is necessary to precisely delineate the contact with the bottom layer, yet such work is beyond the scope of this study.

The inversion of sounding T011, collected in a resistive environment, shows negligible differences between inversions conducted with and without accounting for polarization effects. Results presented in Fig. 5d shows that the first layer consist of two electrical sub-layers, extending to a depth of ca. 7 m, with conductivity values ca. 1.5 mS/m. When polarization effects are considered (Fig. 5e), the thickness of the layer increases, extending to ca. 16 m. The second unit is found between ca. 7 m and 90 m depth. In the real-valued inversion (Fig. 5d), this unit is composed of three sub-layers with an average conductivity of ca. 1 mS/m, typical of metamorphic rocks without graphite. When polarization is included (Fig. 5e), the unit differentiates into two distinct components: (a) an upper section between 16 m and 74 m depth with consistent conductivity values (ca. 1 mS/m) and (b) a lower section from 74 m to 100 m with increased conductivity (ca. 18 mS/m) and measurable polarization (0.1 rad, see Fig. 5f). Due to the low conductivity, the low polarization values observed cannot be interpreted as low graphite content; this layer is related to different polarization mechanisms, as electrical conductivity and capacitive properties also depend on factors such as rock porosity and the surface area of polarizable materials (e.g., clay, organic matter) exposed to electrolytes in pore spaces (Sharifi et al., 2024). The contact with the third layer at depth is poorly resolved, as indicated by the DOI in Fig. 5d, with reliable resolution restricted to the upper 80 m. Despite this limitation, both inversion methods identify a contact at ca. 100 m depth with a material exhibiting higher electrical conductivity, which likely corresponds to weathered metamorphic rocks, such as pyroxene amphibolite (unit 33; c.f., Fig. 1).

The observed increase in polarization values at depth in both soundings is difficult to interpret without borehole data to clarify the distribution of polarizable materials in the subsurface. Additionally, the decrease in sensitivity with depth should be considered, as reported by Aigner et al. (2024), who suggested that transitions from resistive to conductive materials result in larger uncertainty regarding the actual conductivity values below the conductive layers (i.e., graphite bearing).

Fig. 5 shows that electrical conductivity reveals consistent variations at depth, even in inversions conducted without accounting for polarization effects, allowing for the interpretation of geological units. Nonetheless, for a quantitative assessment of graphite content, TEM data must be interpreted with polarization effects included. The same analysis was applied to soundings L035 and L017. L035 corresponds to a polarizable unit within a conductive medium, whereas L017 represents resistive, non-polarizing metamorphic rocks. Results are shown in Appendix A.1 (Fig. A1).

Recent studies have quantitatively interpreted the conductivity and polarization properties in electrical measurements. Revil et al. (2015, 2017, 2022) established a linear relationship between graphite content and polarization effects based on laboratory experiments with grains containing disseminated graphite. Katona et al. (2024) expanded on this by incorporating different grain sizes and rock plugs, applying these laboratory findings to field data collected using electrical methods, specifically induced polarization (IP). Wu and Peruzzo (2020) further demonstrated that the volumetric concentration of graphite significantly affects its polarization signal due to the interconnection and aggregation of particles, which reduce the specific surface area of smaller particles and shift phase responses to lower frequencies. The shift to low-frequency responses (<100 Hz) may explain the minimal changes observed in conductivity models when polarization effects are

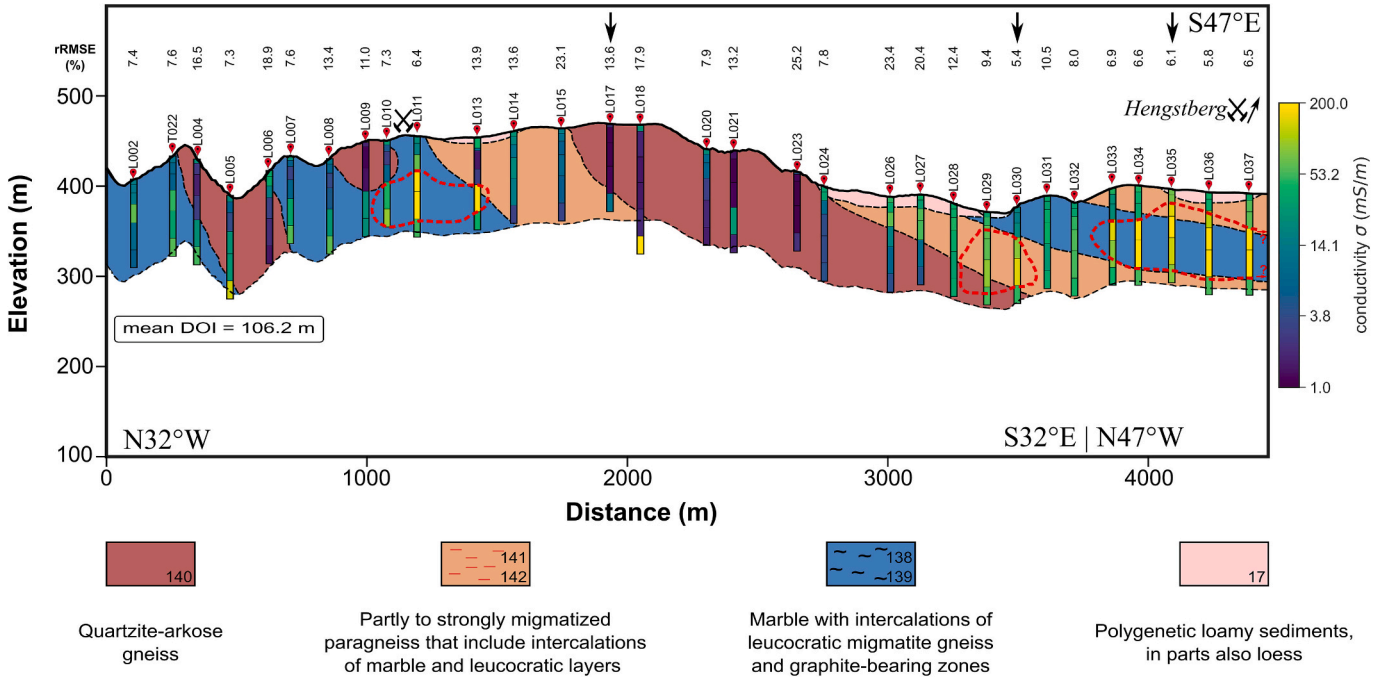

Fig. 6. TEM inversion results along LP2 (GC B-B'). The black line indicates the topography along the profile, while red symbols and labels mark the positions and names of the soundings. The two black markers at approximately 1100 m and 4300 m along the profile denote former graphite mine locations. The dashed black line at the bottom represents the average DOI. The black downward-pointing arrows indicate the soundings mentioned in the previous sections. The background illustrates the geological interpretation of the section based on geophysical data, with red dashed polygons highlighting identified graphite-rich zones. (For interpretation of the references to colour in this figure legend, the reader is referred to the web version of this article.)

considered in electromagnetic surveys, which are typically conducted in the kHz range. This finding aligns with Mörbe et al. (2024), who, in a graphite exploration study in the Kropfmühl area of the Bavarian Mountains, Germany, used large-scale 3D inversions of semi-airborne electromagnetic data. They concluded that polarization effects do influence observed field data, yet such effects do not significantly alter the reconstructed conductivity distribution. The conclusions drawn by Mörbe et al. (2024) are consistent with our observations and support the interpretation of the TEM data presented before. Therefore, the petrophysical models derived from electrical methods are not directly

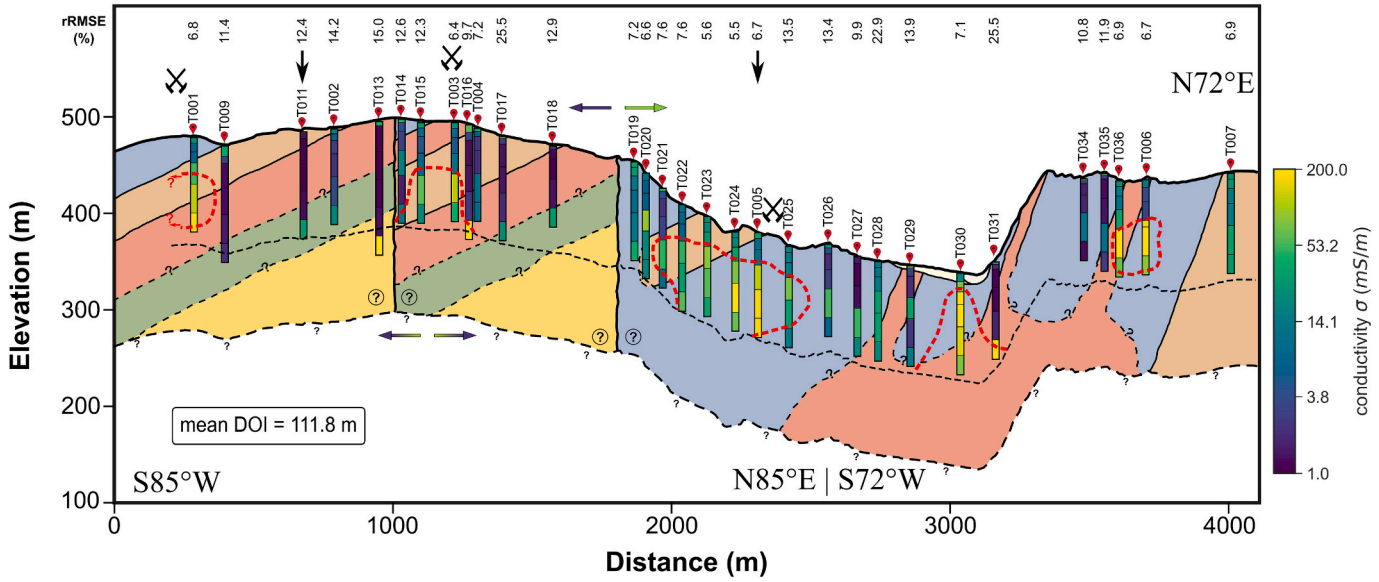

Fig. 7. TEM inversion results along LP1 (GC A-A'). The black line depicts the topography along the profile, with red symbols and labels indicating sounding positions and names. Black markers at approximately 250 m, 1250 m, and 2400 m denote former graphite mine locations. The dashed black line in the middle represents the mean DOI value. The black downward-pointing arrows indicate the soundings mentioned in the previous sections. The background features the geological interpretation based on surface geological data. Black vertical lines at 1000 m and 1800 m indicate fault positions identified from geological information, with gradient-colored horizontal arrows showing adjustments of the first fault (marked at 1000 m) based on geophysical contrasts. The second pair of horizontal arrows highlight the significant lateral change in conductivity across the second fault (marked at 1800 m), with lower values (<5 mS/m; dark arrow) to the southwest and higher values (>30 mS/m; light arrow) to the northeast. Red dashed polygons outline identified graphite-rich areas. (For interpretation of the references to colour in this figure legend, the reader is referred to the web version of this article.)

applicable for interpreting electromagnetic methods and require further investigation, which falls outside the scope of this study.

3.4. Geological cross-sections enhanced by geophysical data

Fig. 6 shows the geoelectrical cross-section B-B' constructed from the inversion results of the 31 TEM soundings collected. Soundings located near documented former graphite mines consistently exhibit rRMSE values below 8 %, while those soundings at other locations revealed rRMSE values up to 25 %. These variations are consistent to the decrease in S/N of highly resistive materials as discussed above for the sounding L017.

In the cross-section presented in Fig. 6, we observe three different zones that exhibit high electrical conductivity (> 100 mS/m), indicative of graphite deposits: (1) at a distance between 1020 m and 1480 m at depths of ca. 40 m to 90 m; (2) between 3280 m and 3580 m at depths of ca. 20 m to 75 m; and (3) between 3780 m to 4400 m at depths between 20 and 75 m. The first and third zones align with the locations of two former graphite mines, where electrical conductivities exceed 200 mS/m. Zone 2 reveals a highly conductive anomaly that could represent a 1.5 km extension to the northwest of the Hengstberg graphite mine, identifying a previously unexplored area of interest. The third zone suggests a continuation of the graphite-rich area mined at Hengstberg, coinciding with the paragneiss-marble contact observed at the 4000 m mark on profile LP2 (Fig. 1, soundings L033-L037).

The geological interpretation of the cross-section, based on geophysical data, is also presented in Fig. 6. This interpretation can be divided into two main parts according to the conductivity of the soundings. From sounding L002 to sounding L024, the subsurface is primarily characterized by lower conductivity values, with occasional zones exceeding 100 mS/m. This part can be interpreted as a sequence of graphite-bearing marble (units 45 and 50 in Mautern and units 138 and 139 in Upper Grafendorf; c.f., Fig. 1) intercalated with quartzite-arkose gneiss (unit 140; c.f., Fig. 1). In contrast, between soundings L024 and L037, the conductivity values are higher, corresponding to a sequence of strongly migmatized paragneiss with intercalated marble and leucocratic layers (units 141 and 142; c.f., Fig. 1), along with graphite-bearing marble (units 138 and 139; c.f., Fig. 1). Additionally, in certain parts of the entire cross-section, the crystalline rock units are overlain by polygenetic loamy sediments, which may include loess deposits (units 6 and 17 in Mautern and Upper Grafendorf, respectively; c.f., Fig. 1).

Fig. 7 presents the TEM results for the LP1 profile overlaid on the GC A-A', which, unlike B-B', was derived from geological mapping rather than geophysical data. This comparison enables us to evaluate our interpretation, particularly regarding the high conductivity values that suggest graphite-rich areas. We categorize the soundings into two groups based on conductivity values. The first group, with low conductivity (<14 mS/m), corresponds to crystalline rocks devoid of graphite-rich zones, associated with pyroxene amphibolite (unit 33; c.f., Fig. 1), leucocratic magmatic gneiss (unit 43; c.f., Fig. 1), and paragneiss (unit 42; c.f., Fig. 1). This interpretation is consistent with the geophysical studies carried out by Aigner et al. (2024) and Katona et al. (2024) in nearby regions, where host rock conductivity was ca. 16 mS/m. In contrast, the second group exhibits high conductivity (100 mS/m

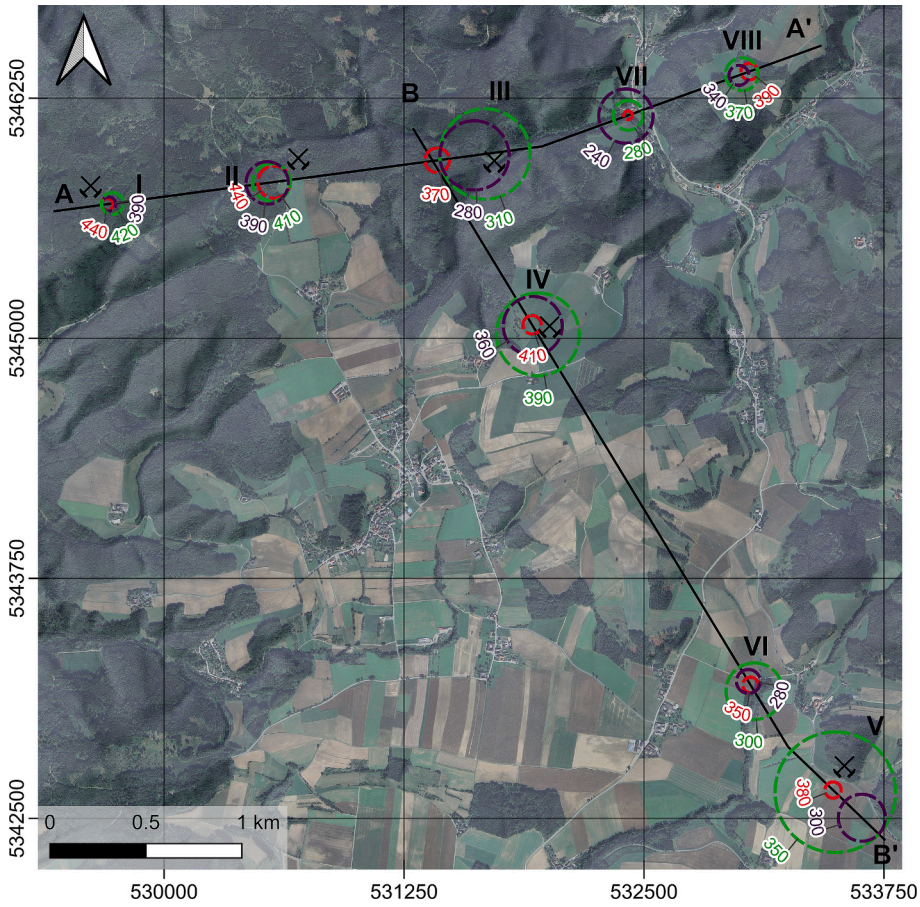

Fig. 8. Map view of graphite-rich areas identified from high-conductivity anomalies observed in both profiles. The dashed colored circles highlight these anomalies at different elevations: red indicates the uppermost extent, green marks the widest lateral spread along the profile, and purple represents the lowest depth reached by our measurements. The lateral extent of the conductivity anomalies perpendicular to the profiles cannot be determined due to the lack of data in that direction. Black symbols indicate known surface occurrences of graphite, including former graphite mines, as reported in geological data. Roman numerals I - VIII denote the different mapped anomalies. (For interpretation of the references to colour in this figure legend, the reader is referred to the web version of this article.)

to 200 mS/m), indicative of electrical conductors related to localized graphite deposits within graphite-bearing paragneiss and marble (units 42 and 50; c.f., Fig. 1), and leucocratic migmatite gneiss with marble intercalations (unit 44; c.f., Fig. 1).

As was discussed for GC B-B' and based on the previous TEM sounding categorization, five different zones of high electrical conductivity (>100 mS/m) indicative of graphite deposits for GC A-A' can also be done as it is done in Fig. 7: (1) ca. 280 m at depths of 50 m to 90 m; (2) between 1060 m and 1240 m at ca. 55 m depth; (3) between 1940 m and 2450 m at depths of 50 m to 130 m; (4) ca. 3030 m at similar depths as the third zone; and (5) between 3585 m and 3740 m at depths of 40 m to 90 m. The first three zones correspond with locations of former graphite mines, where electrical conductivities exceed 200 mS/m. Zones 4 and 5 reveal highly conductive anomalies that may represent unexplored areas of interest.

Fig. 7 also highlights two faults at 1000 m and 1800 m along the GC A-A'. However, for the first fault, due to the significant conductivity contrast observed around TEM soundings T013 and T016, we propose adjusting the position of the fault to this area. The second fault aligns well with the conductivity contrast zones around TEM soundings T018-T019. Soundings on both sides of the fault zones generally exhibit good data quality, with the inversion achieving acceptable rRMSE values (< 15 %). Notably, there is a marked lateral change in conductivity, with lower values (< 5 mS/m) to the southwest and higher values (>30 mS/m) to the northeast of the second fault. The interpretation of these lateral discontinuities as faults aligns with the study by Zhu et al. (2024), which identified fault locations based on the distribution of resistivity models and characterized them as zones with low resistivity values.

A notable difference in the geological interpretations of the two cross-sections concerns the representation of subsurface layers. In GC B-B', the rock layers appear to dip southeast (Fig. 6), whereas in GC A-A', they appear to dip southwest (Fig. 7). This discrepancy arises from the negative angle of the structural bearing (β; $-8°$ and $-23°$), which occurs because the compass bearing angle (θ; 133° and 148°) exceeds the structural strike (S; 125°). According to Herold's (1933) trigonometric equation, this negative β results in a negative apparent dip (α), suggesting that although the layers in GC B-B' seem to dip southeast, they are actually dipping southwest. This southwest dip aligns with the overall geological trend of the study area. Therefore, to accurately represent the true dip direction (δ), the layers must be depicted in the

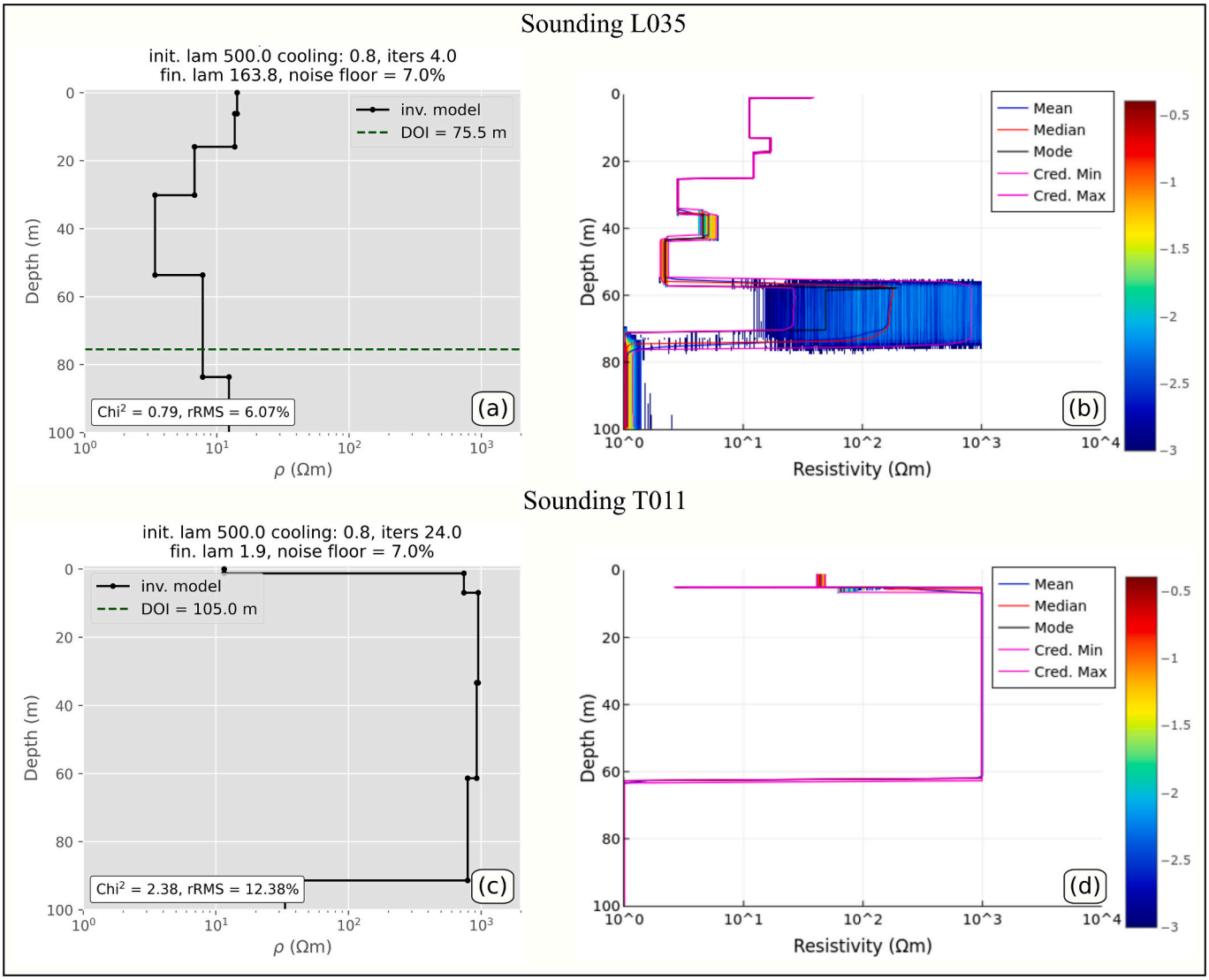

Fig. 9. Comparison of TEM inversion results in terms of electrical resistivity for two soundings: L035 from profile LP2 and T011 from profile LP1. Results are shown using the inversion code by Aigner et al. (2024) (a and c) and the TransdEM software by Peng et al. (2022) (b and d). Sounding L035 (a-b) is located at a former graphite mine, while sounding T011 (c-d) is in an area where no significant graphite content is expected. (a and c) show the resistivity model as a function of depth. (b and d) depict the posterior probability density of resistivity with depth.

opposite direction. Proper consideration of this factor is crucial for accurate geological interpretation, as overlooking it may lead to errors in identifying and delineating graphite-rich areas.

As shown in Figs. 6 and 7, high conductivity anomalies are primarily associated with the lithological contacts between units such as graphite-bearing marble, leucocratic migmatite gneiss with marble intercalations, and graphite-bearing paragneiss with intercalated marble. This observation aligns with findings by Simandl et al. (2015), who reported that the highest graphite grades in paragneiss-hosted deposits are often located near these contacts. Additionally, they identified that paragneiss and marble rocks subjected to upper amphibolite to granulite facies metamorphism are the most common hosts for economically significant crystalline flake graphite deposits. In the case of the Hengstberg area, it is known that this region experienced such metamorphism during the Variscan Orogeny – the final collision between Gondwana and Laurussia supercontinents (Kroner et al., 2008). This geological history, documented by Weber et al. (2019), exemplifies the relationship between these metamorphic conditions and the presence of flake graphite deposits.

Based on the TEM conductivity models, we propose graphite-rich zones along both profiles, which are presented in Fig. 8. The zones I to V coincide with the locations of former graphite mines, validating our interpretation. Accordingly, our study suggests that the zones VI, VII and VIII are potential areas to exploit graphite at depths ranging between 20 m and 80 m.

3.5. Assessing the uncertainty of electrical resistivity models retrieved from TEM data

Up to this point, our interpretation has been based on electrical conductivity values, providing insights into the location and geometry of potential graphite-rich zones. To assess the reliability of our electrical characterization, in this section we discuss our results in comparison to models obtained using the TransdEM software (Peng et al., 2022). To highlight that the results are obtained with a different algorithm, they are presented here in terms of electrical resistivity, which is the standard parameter output by TransdEM (Fig. 9).

Fig. 9b and d show that the posterior probability density function (PDF) of electrical resistivity captures most of the features present in our inversion models of soundings L035 and T011 (Fig. 9a and c; respectively). The 90 % credible interval of the PDF further confirms that transitions from a conductive to a resistive layer reduce signal strength, whereas transitions from a resistive to a conductive layer enhance sensitivity due to the presence of conductive material at depth, as discussed earlier in the TEM inversion analysis. In Fig. 9b, the resistive structure observed at ca. 60 m depth is associated with increased uncertainty in resistivity estimates, reflected by the broader posterior PDF due to limited data sensitivity. In contrast, Fig. 9d displays a narrower credible interval, indicating higher sensitivity. This aligns with the well-established capability of the TEM method to achieve higher resolution in conductive layers (e.g., Raiche et al., 1985).

Based on the inversion results from both algorithms, sounding L035 can be described as a three-layer model. As shown in Fig. 9a and b, the electrical resistivity values of the different layers are similar between both approaches, with the main differences occurring at the top or bottom boundaries (i.e., layer thicknesses). The first layer has a resistivity of ca. 15 Ωm, with a thickness difference of ca. 5 m between the models. The second layer shows a resistivity of ca. 5 Ωm, with a variation of ca. 5 m in its top boundary, while the bottom boundary is consistent across both algorithms (ca. 55 m depth). The third layer shows an increase in resistivity in both approaches, which may result in reduced sensitivity due to the transition from a conductive to a resistive medium, as previously discussed. Despite this, the variation in thickness is minor, ca. 5 m. Sounding T011 can be interpreted as a two-layer model. As observed in Fig. 9c and d, the main difference lies in the depth of the bottom interface of the first layer, which varies by ca. 20 m. This variation is attributed to the lower sensitivity in resistive settings. Overall, the resistivity models from both algorithms agree on the main contrasts between conductive and resistive layers, supporting the consistency and robustness of our interpretations.

The same analysis was applied to soundings T005 and L017. T005 corresponds to a conductive setting (similar to L035), while L017 represents a resistive environment (comparable to T011). These results are presented in Appendix A.2 (Fig. A2). Further supporting this comparison, Fig. A3 (Appendix A.2) shows the posterior distributions of layer interface depths (Fig. A3c and e) and histograms of the number of layers for all posterior models (Fig. A3d and f).

4. Conclusions

Our findings demonstrate that GCs are valuable tools for understanding the shallow subsurface. However, their limitations become apparent when interpreting the extent and location of deeper deposits of critical raw material, such as graphite. Our results highlight the strength of the TEM method in enhancing GCs based on geological information by incorporating changes derived from the electrical properties of the subsurface. TEM proves to be a rapid and efficient tool for mapping large areas in the search for graphite deposits, making it particularly well-suited for investigations in abandoned mining areas and unexplored regions. The approach presented here is well suited for locations where access is difficult due to the absence of roads and dense vegetation, where continuous collection (i.e., TEM towed by vehicles) would not be possible.

While neglecting polarization effects in the inversion process could lead to inaccurate electrical conductivity values, our study reveals that polarization has only a minor impact on the overall conductivity models derived from TEM data. Although some differences are observed, these do not significantly alter the qualitative interpretation of geological structures at a large scale. This suggests that, in many cases, inversions of TEM data without considering polarization effects can still provide reliable insights into the geometry and distribution of geological formations. This conclusion is further supported by our comparison with independent inversions obtained with TransdEM. Despite differences in methodological frameworks, the results obtained from the MCMC approach were consistent with our inversion models, supporting our interpretations. However, accurately quantifying graphite content will require future studies to integrate IP parameters into the inversion process. The petrophysical model linking graphite content and the conductivity and polarization responses in TEM data remains an open area of research.

The anomalous high-conductivity structures identified in the subsurface, validated by numerical experiments, show a sharp contrast with the surrounding high-resistivity rocks. These numerical experiments provide critical insight by simulating the electromagnetic response of different subsurface scenarios, allowing us to confirm that the device used in this study is capable of accurately measuring highly conductive anomalies as expected for graphite rich areas. Some of these underground anomalies correlate with known surface occurrences of graphite reported in geological data, strengthening the validity of our interpretations. The association of these anomalies with paragneiss and marble contacts strongly suggests a high potential for flake-type graphite deposits in Lower Austria. This finding underscores the need for further exploration to assess the depth extension of these deposits, especially beyond 30 m of depth, in areas with historical mining activity.

CRediT authorship contribution statement

Jorge Luis Monsalve Martínez: Writing – original draft, Writing – review & editing, Visualization, Validation, Methodology, Investigation, Formal analysis, Data curation, Conceptualization. **Lukas Aigner:** Writing – review & editing, Software, Methodology, Investigation, Conceptualization. **Philipp Högenauer:** Writing – review & editing,

Investigation. **Adrián Flores Orozco:** Writing – review & editing, Validation, Supervision, Resources, Project administration, Methodology, Investigation, Conceptualization.

Declaration of competing interest

The authors declare that they have no known competing financial interests or personal relationships that could have appeared to influence the work reported in this paper.

Acknowledgements

This research work was co-financed by the Federal Ministry of education, science and research and supervised by the Federal Mining Authority of Austria within the framework of the VLG83 project (Raw Material research initiative). The authors acknowledge TU Wien Bibliothek for financial support through its Open Access Funding Programme.

Appendix A

A.1. Considering polarization effects in TEM data for graphite quantification

Fig. A1 presents a comparison of inversion results for soundings L035 and L017, with and without considering polarization effects. These soundings reflect distinct geological settings: L035 corresponds to a polarizable unit within a conductive medium, suggesting the presence of graphite (similar to sounding T005), whereas L017 represents resistive, non-polarizing metamorphic rocks devoid of graphite (comparable to sounding T011). As previously discussed, the overall structure of the electrical conductivity models remains largely unchanged between the two inversion approaches. The observed increase in polarization values at greater depths is challenging to interpret without borehole data to confirm the distribution of polarizable materials. Furthermore, the reduction in sensitivity with depth must be considered, as noted by Aigner et al. (2024), who highlighted that conductivity transitions from resistive to conductive layers introduce greater uncertainty in determining subsurface conductivity values. For a more precise evaluation of graphite content, TEM data should be analyzed while accounting for polarization effects.

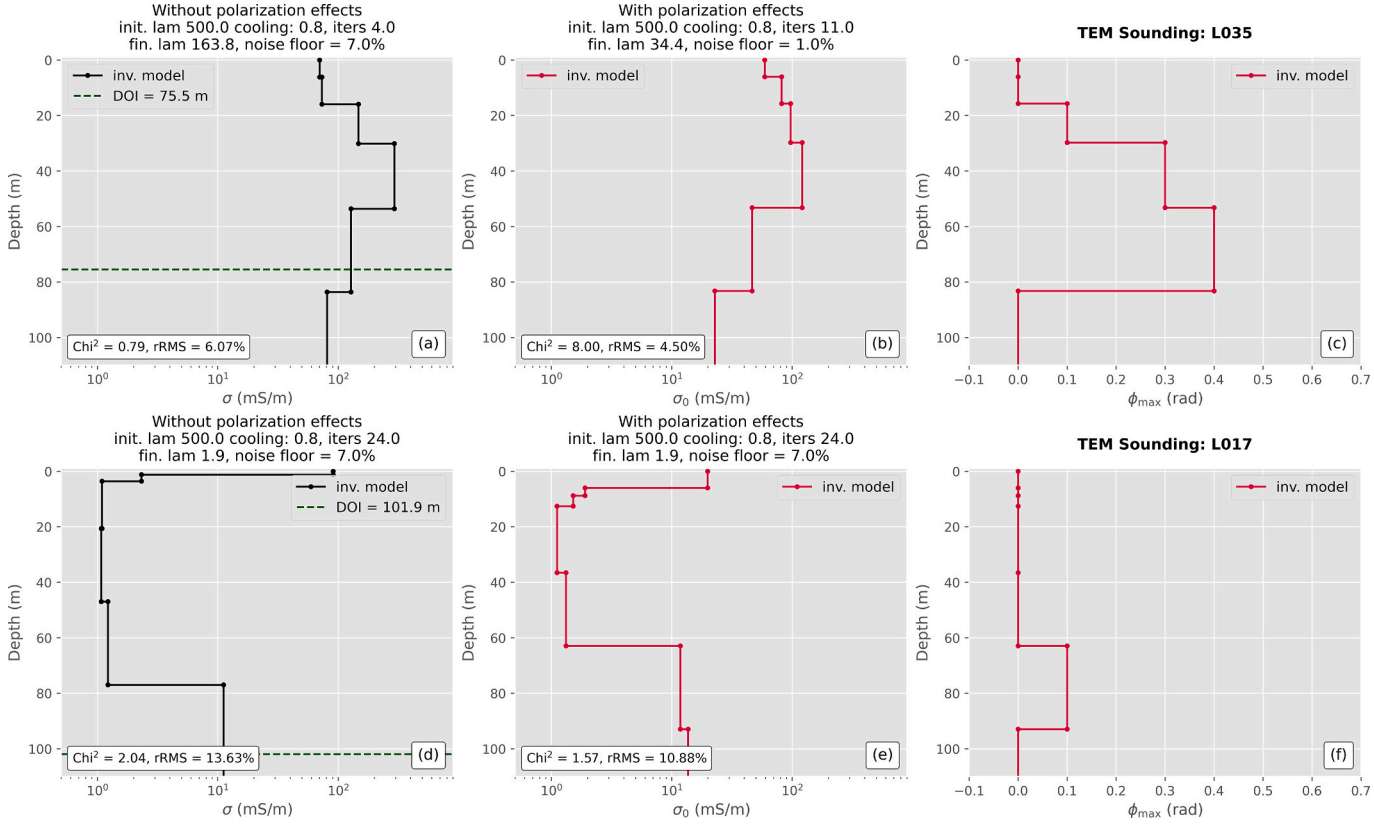

Fig. A1. Comparison of TEM inversion results for two sounding positions from profile LP2 without (a and d) and with polarization effects (b-c and e-f). Sounding position L035 (a-c) corresponds to a former graphite mine, and sounding position L017 (d-f) corresponds to a location where no significant graphite content is expected in the subsurface.

A.2. Assessing the uncertainty of electrical resistivity models retrieved from TEM data

Fig. A2 evaluates the reliability of our inversion results by comparing the posterior PDF of electrical resistivity with our inversion models for two additional soundings: T005 (Fig. A2a) and L017 (Fig. A2c). The posterior PDF in Fig. A2b and d capture resistivity features observed in our inversion models. As discussed earlier, the transition from a conductive to a resistive layer leads to reduced signal sensitivity, which is reflected in the broader 90 % credible intervals of the posterior PDF. In Fig. A2b, the increased uncertainty in resistivity estimates is evident in the resistive structures observed at depths of ca. 45 to 62 m and ca. 70 to 85 m. In opposition, when transitioning from a resistive to a conductive layer, sensitivity increases due to the presence of highly conductive material at depth, leading to a more constrained credible interval, as observed in Fig. A2d. Fig. A3 (a-b for T005 and g-h

for L017) presents, for both soundings, the posterior distributions of layer interface depths (Fig. A3a and g) and histograms of the number of layers for all posterior models (Fig. A3b and h).

For sounding T005, the results from both algorithms suggest a two-layer model. As shown in Fig. A2a and b, the first layer is resistive, with a bottom boundary consistently located ca. 38 m. In our model (Fig. A2a), the second layer is characterized by a conductive unit (ca. 8 Ωm) extending down to ca. 90 m. This conductive feature is also captured in the TransdEM results (from ca. 38 to ca. 45 m in Fig. A2b), although followed by zones of higher resistivity with increased uncertainty between ca. 45 and ca. 85 m, coinciding with the transition to resistive material and the corresponding drop in sensitivity. For sounding L017, also interpreted as a two-layer model, the main difference between approaches lies in the depth of the first interface, which differs by approximately 18 m (Fig. A2c and d). This variation is consistent with the reduced resolution typically seen in resistive environments. Despite these differences, both inversion methods agree on the contrasts between conductive and resistive zones, lending credibility to our overall interpretation.

Fig. A3(a, c, e, and g) illustrates that the upper boundary of conductive layers is better resolved than the lower boundary, particularly when there is a transition from a highly resistive structure to a conductive one. This is evident from the probability peaks aligning more closely with the top interface position. Additionally, Fig. A3(b, d, f, and h) shows that models dominated by resistive structures tend to have fewer probable layers compared to models with conductive layers. This behavior reflects the characteristic sensitivity of the TEM method, which responds more strongly to the overall conductance of a conductive layer rather than to its individual conductivity or thickness (Blatter et al., 2018).

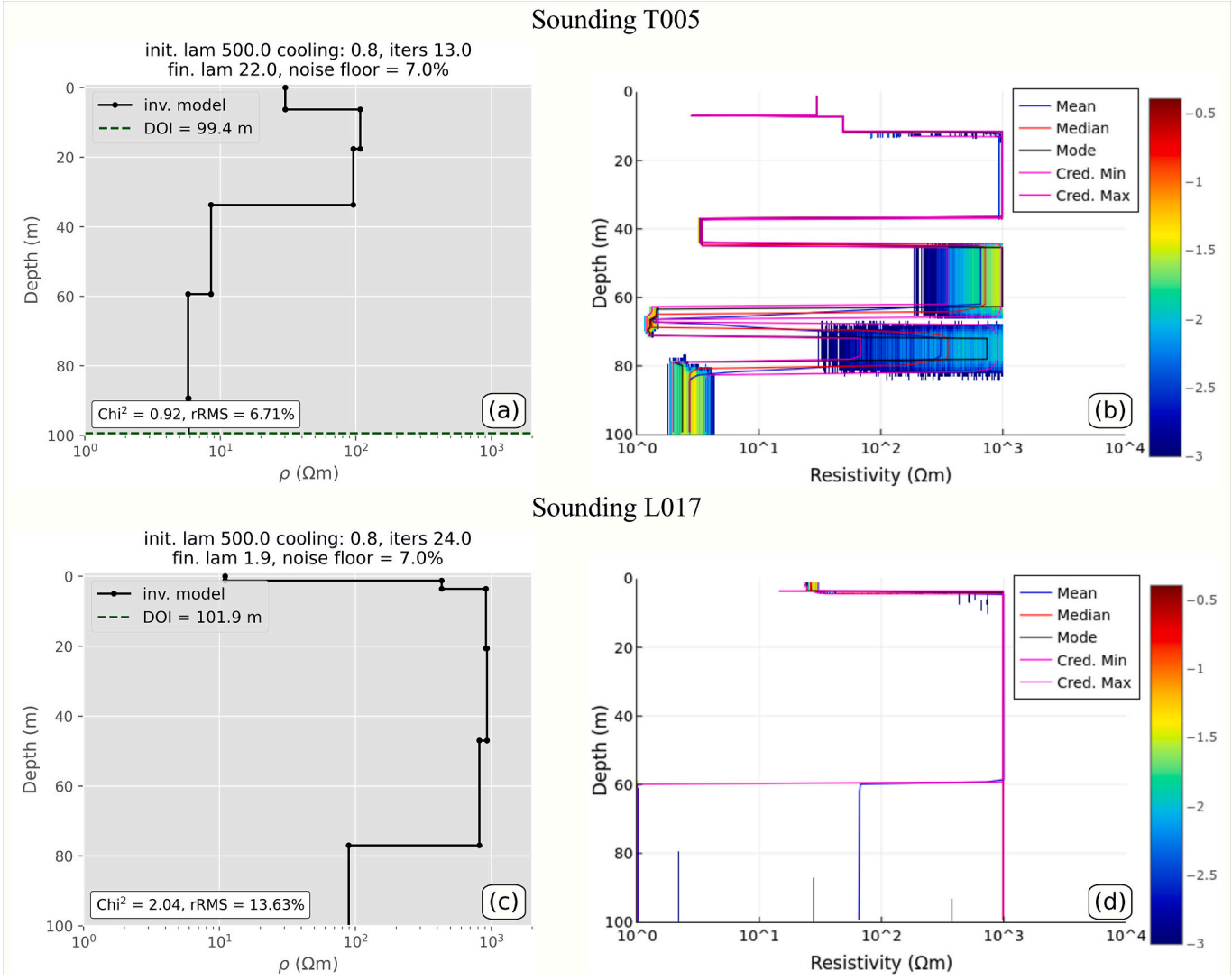

Fig. A2. Comparison of TEM inversion results in terms of electrical resistivity for two soundings: T005 from profile LP1 and L017 from profile LP2. Results are shown using the inversion code by Aigner et al. (2024) (a and c) and the TransdEM software by Peng et al. (2022) (b and d). Sounding T005 (a-b) is located at a former graphite mine, while sounding L017 (c-d) is in an area where no significant graphite content is expected. (a and c) display the resistivity model as a function of depth. (b and d) show the posterior probability density of resistivity with depth.

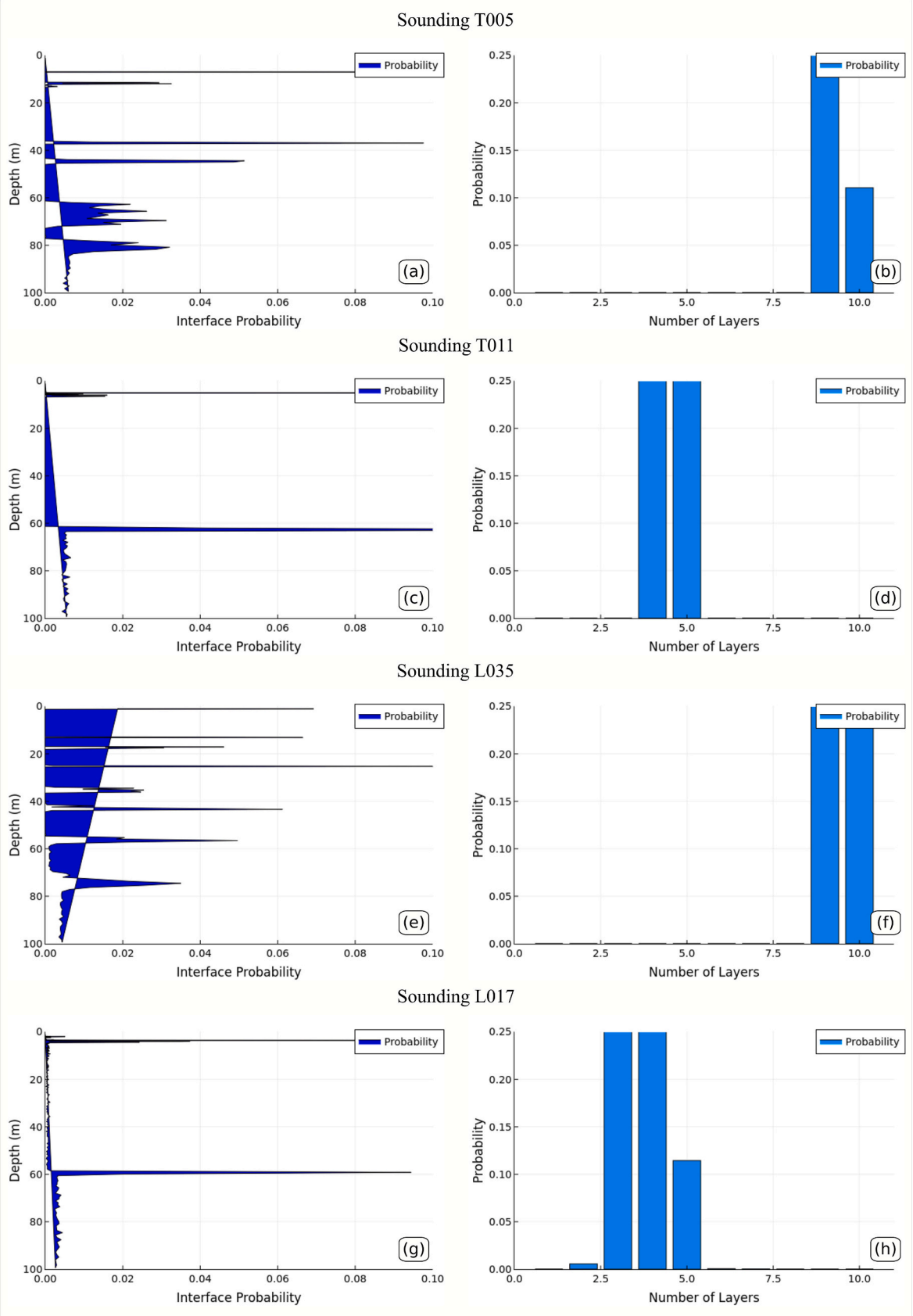

Fig. A3. Posterior distributions of layer interface depths (a, c, e, g) and histograms of the number of layers in all posterior models (b, d, f, h) obtained using the TransdEM software by Peng et al. (2022) for four soundings: T005 (a-b) and T011 (c-d) from profile LP1, and L035 (e-f) and L017 (g-h) from profile LP2. Soundings T005 and L035 are located at former graphite mines, whereas soundings T011 and L017 correspond to areas where no significant graphite content is expected.

Data availability

Data associated with this research are available and can be obtained by contacting the corresponding author.

References

Agostinetti, N.P., Malinverno, A., 2010. Receiver function inversion by trans-dimensional Monte Carlo sampling. Geophys. J. Int. 181 (2), 858–872. https://doi.org/10.1111/j.1365-246X.2010.04530.x.

Aigner, L., Högenauer, P., Bücker, M., Flores Orozco, A., 2021. A flexible single loop setup for water-borne transient electromagnetic sounding applications. Sensors 21 (19), 6624. https://doi.org/10.3390/s21196624.

Aigner, L., Werthmüller, D., Flores Orozco, A., 2024. Sensitivity analysis of inverted model parameters from transient electromagnetic measurements affected by induced polarization effects. J. Appl. Geophys. 223, 105334. https://doi.org/10.1016/j.jappgeo.2024.105334.

Auken, E., Foged, N., Larsen, J.J., Lassen, K.V.T., Maurya, P.K., Dath, S.M., Eiskjær, T.T., 2019. tTEM – a towed transient electromagnetic system for detailed 3D imaging of the top 70 m of the subsurface. Geophysics 84 (1), E13–E22. https://doi.org/10.1190/geo2018-0355.1.

Bezanson, J., Edelman, A., Karpinski, S., Shah, V.B., 2017. Julia: a fresh approach to numerical computing. SIAM Rev. 59 (1), 65–98. https://doi.org/10.1137/141000671.

Binley, A., Hubbard, S.S., Huisman, J.A., Revil, A., Robinson, D.A., Singha, K., Slater, L. D., 2015. The emergence of hydrogeophysics for improved understanding of subsurface processes over multiple scales. Water Resour. Res. 51 (6), 3837–3866. https://doi.org/10.1002/2015WR017016.

Blatter, D., Key, K., Ray, A., Foley, N., Tulaczyk, S., Auken, E., 2018. Trans-dimensional Bayesian inversion of airborne transient EM data from Taylor Glacier, Antarctica. Geophys. J. Int. 214 (3), 1919–1936. https://doi.org/10.1093/gji/ggy255.

Bücker, M., Flores Orozco, A., Kemna, A., 2018. Electrochemical polarization around metallic particles – part 1: the role of diffuse-layer and volume-diffusion relaxation. Geophysics 83 (4), E203–E217. https://doi.org/10.1190/geo2017-0401.1.

Bücker, M., Flores Orozco, A., Undorf, S., Kemna, A., 2019. On the role of Stern-and diffuse-layer polarization mechanisms in porous media. J. Geophys. Res. Solid Earth 124 (6), 5656–5677. https://doi.org/10.1029/2019JB017679.

Bücker, M., Flores Orozco, A., Gallistl, J., Steiner, M., Aigner, L., Hoppenbrock, J., Glebe, R., Morales Becerra, W., Pita de la Paz, C., García García, C.E., Razo Pérez, J. A., Buckel, J., Hördt, A., Schwalb, A., Pérez, L., 2021. Integrated land and water-borne geophysical surveys shed light on the sudden drying of large karst lakes in southern Mexico. Solid Earth 12 (2), 439–461. https://doi.org/10.5194/se-12-439-2021.

Christiansen, A.V., Auken, E., Sørensen, K., 2006. The transient electromagnetic method. In: Groundwater Geophysics: A Tool for Hydrogeology. Springer Berlin Heidelberg, Berlin, Heidelberg, pp. 179–225.

Damm, S., 2021. Rohstoffrisikobewertung - Graphit: Berlin, DERA. In: DERA rohstoffinformationen, 51, p. 1116.

Ellis, R.G., 1998. Inversion of airborne electromagnetic data. Explor. Geophys. 29 (2), 121–127. https://doi.org/10.1071/EG998121.

European Commission, 2020. Study on the EU's List of Critical Raw Materials (2020) – Final Report. https://doi.org/10.2873/11619.

European Parliament and Council of the EU, 2024. Regulation (EU) 2024/1252 of 11 April 2024 Establishing a Framework for Ensuring a Secure and Sustainable Supply of Critical Raw Materials and Amending Regulations (EU) No 168/2013, (EU) 2018/858, (EU) 2018/1724 and (EU) 2019/1020. http://data.europa.eu/eli/reg/2024/1252/oj.

Fiandaca, G., Madsen, L.M., Maurya, P.K., 2018. Re-parameterisations of the Cole–Cole model for improved spectral inversion of induced polarization data. Near Surf. Geophys. 16 (4), 385–399. https://doi.org/10.3997/1873-0604.2017065.

Fitterman, D.V., Anderson, W.L., 1987. Effect of transmitter turn-off time on transient soundings. Geoexploration 24 (2), 131–146. https://doi.org/10.1016/0016-7142(87)90087-1.

Flores, C., Peralta-Ortega, S.A., 2009. Induced polarization with in-loop transient electromagnetic soundings: a case study of mineral discrimination at El Arco porphyry copper, Mexico. J. Appl. Geophys. 68 (3), 423–436. https://doi.org/10.1016/j.jappgeo.2009.03.009.

Fossen, H., 2010. Structural Geology, first ed. Cambridge University Press, New York.

Galdón, J.M., Rey, J., Martínez, J., Hidalgo, M.C., 2017. Application of geophysical prospecting techniques to evaluate geological-mining heritage: the Sinapismo mine (La Carolina, Southern Spain). Eng. Geol. 218, 152–161. https://doi.org/10.1016/j.enggeo.2017.01.012.

Gautneb, H., Gloaguen, E., Törmänen, T., Bertrand, G., Sadeghi, M., Schedl, A., Pfleiderer, S., Lucarini, M., 2020a. ELIVERABLE D5.1. Title Provide Mineral Potential and Prospectivity Maps of Key Mineral Provinces in Europe with Deposits of, or Potential for, Energy Critical Elements (Natural Graphite, Lithium, Cobalt) in Collaboration. https://doi.org/10.13140/RG.2.2.29880.67844.

Gautneb, H., Rønning, J.S., Engvik, A.K., Henderson, I.H., Larsen, B.E., Solberg, J.K., Ofstad, F., Gellein, J., Elvebakk, H., Davidsen, B., 2020b. The graphite occurrences of northern Norway, a review of geology, geophysics, and resources. Minerals 10 (7), 626. https://doi.org/10.3390/min10070626.

Gautneb, H., Rønning, J.S., Larsen, B.E., 2023. A Step Towards Meeting Battery Raw Material Demand: The Geology and Exploration of Graphite Deposits, Examples from Northern Norway. https://doi.org/10.1144/SP526-2021-180.

Green, P.J., 1995. Reversible jump Markov chain Monte Carlo computation and Bayesian model determination. Biometrika 82 (4), 711–732. https://doi.org/10.1093/biomet/82.4.711.

Harris, B.D., Wilkes, P.G., Kepic, A., 2006. Acquisition of very early time transient electromagnetic data for shallow geotechnical, environmental and hydrogeological applications. In: Symposium on the Application of Geophysics to Engineering and Environmental Problems 2006. Society of Exploration Geophysicists, pp. 631–638. https://doi.org/10.4133/1.2923701.

Hatherly, P., 2013. Overview on the application of geophysics in coal mining. Int. J. Coal Geol. 114, 74–84. https://doi.org/10.1016/j.coal.2013.02.006.

Herold, S.C., 1933. Projection of dip angle on profile section. Am. Assoc. Pet. Geol. Bull. 17, 740–742.

Hofbauer, R., 1995. 36 Jahre Grafitabbau der Firma Industrie & Bergbaugesellschaft Pryssok & Co. KG im Niederösterreichischen Waldviertel. Zeitschrift des Montanhistorischen Vereins für Österreich 11, 28–31.

Kaipio, J.P., Kolehmainen, V., Somersalo, E., Vauhkonen, M., 2000. Statistical inversion and Monte Carlo sampling methods in electrical impedance tomography. Inverse Probl. 16 (5), 1487. https://doi.org/10.1088/0266-5611/16/5/321.

Kang, S., Oldenburg, D.W., Heagy, L.J., 2020. Detecting induced polarisation effects in time-domain data: a modelling study using stretched exponentials. Explor. Geophys. 51 (1), 122–133. https://doi.org/10.1080/08123985.2019.1690393.

Katona, T., Flores-Orozco, A., Aigner, L., Benold, C., 2024. Graphite content identification with laboratory and field spectral induced polarization measurements. Appl. Sci. 14 (10), 3955. https://doi.org/10.3390/app14103955.

Killingbeck, S.F., Booth, A.D., Livermore, P.W., Bates, C.R., West, L.J., 2020. Characterisation of subglacial water using a constrained transdimensional Bayesian transient electromagnetic inversion. Solid Earth 11 (1), 75–94. https://doi.org/10.5194/se-11-75-2020.

Kroner, U., Mansy, J.L., Mazur, S., Aleksandrowski, P., Hann, H.P., Huckriede, H., Lacquement, F., Lamarche, J., Ledru, P., Pharaoh, T.C., Zedler, H., Zeh, A., Zulauf, G., 2008. Variscan Tectonics. https://doi.org/10.1144/CEV1P.11.

Lane Jr., J.W., Briggs, M.A., Maurya, P.K., White, E.A., Pedersen, J.B., Auken, E., Terry, N., Minsley, B., Kress, W., LeBlanc, D.R., Adams, R., Johnson, C.D., 2020. Characterizing the diverse hydrogeology underlying rivers and estuaries using new floating transient electromagnetic methodology. Sci. Total Environ. 740, 140074. https://doi.org/10.1016/j.scitotenv.2020.140074.

Marescot, L., Monnet, R., Chapellier, D., 2008. Resistivity and induced polarization surveys for slope instability studies in the Swiss Alps. Eng. Geol. 98 (1–2), 18–28. https://doi.org/10.1016/j.enggeo.2008.01.010.

Martín, S., Uzkeda, H., Poblet, J., Bulnes, M., Rubio, R., 2013. Construction of accurate geological cross-sections along trenches, cliffs and mountain slopes using photogrammetry. Comput. Geosci. 51, 90–100. https://doi.org/10.1016/j.cageo.2012.09.014.

Maurya, P.K., Grombacher, D., Lind, J., Lane, J.W., Auken, E., 2022. Inversion of induced polarization-affected towed-transient electromagnetic data in a lateritic regolith geology: a case study from western Tanzania. Geophysics 87 (4), B247–B254. https://doi.org/10.1190/geo2021-0396.1.

Mogi, T., Kusunoki, K.I., Kaieda, H., Ito, H., Jomori, A., Jomori, N., Yuuki, Y., 2009. Grounded electrical-source airborne transient electromagnetic (GREATEM) survey of Mount Bandai, North-Eastern Japan. Explor. Geophys. 40 (1), 1–7. https://doi.org/10.1071/EG08115.

Mörbe, W., Yogeshwar, P., Tezkan, B., Kotowski, P., Thiede, A., Steuer, A., Rochlitz, R., Günther, T., Brauch, K., Becken, M., 2024. Large-scale 3D inversion of semi-airborne electromagnetic data-topography and induced polarization effects in a graphite exploration scenario. Geophysics 89 (5), 1–54. https://doi.org/10.1190/geo2023-0471.1.

Mosegaard, K., Tarantola, A., 1995. Monte Carlo sampling of solutions to inverse problems. J. Geophys. Res. Solid Earth 100 (B7), 12431–12447. https://doi.org/10.1029/94JB03097.

Nagendran, R., 2024. Explicit observation of tertiary magnetic field in TDEM transients; plausible explanation towards induced polarization effect in geophysical prospecting. J. Appl. Geophys. 226, 105402. https://doi.org/10.1016/j.jappgeo.2024.105402.

Olhoeft, G.R., 1985. Low-frequency electrical properties. Geophysics 50 (12), 2492–2503. https://doi.org/10.1190/1.1441880.

Pelton, W.H., Ward, S.H., Hallof, P.G., Sill, W.R., Nelson, P.H., 1978. Mineral discrimination and removal of inductive coupling with multifrequency IP. Geophysics 43 (3), 588–609. https://doi.org/10.1190/1.1440839.

Peng, R., Han, B., Liu, Y., Hu, X., 2022. A Julia software package for transdimensional Bayesian inversion of electromagnetic data over horizontally stratified media. Geophysics 87 (5), F55–F66. https://doi.org/10.1190/geo2021-0534.1.

Puzyrev, V., 2019. Deep learning electromagnetic inversion with convolutional neural networks. Geophys. J. Int. 218 (2), 817–832. https://doi.org/10.1093/gji/ggz204.

Ragan, D.M., 2009. Structural Geology, an Introduction to Geometrical Techniques, fourth ed. Cambridge University Press, New York.

Raiche, A.P., 1984. The effect of ramp function turn-off on the TEM response of layered earth. Explor. Geophys. 15 (1), 37–41. https://doi.org/10.1071/EG984037.

Raiche, A.P., Jupp, D.L.B., Rutter, H., Vozoff, K., 1985. The joint use of coincident loop transient electromagnetic and Schlumberger sounding to resolve layered structures. Geophysics 50 (10), 1618–1627. https://doi.org/10.1190/1.1441851.

Ray, A., Key, K., Bodin, T., Myer, D., Constable, S., 2014. Bayesian inversion of marine CSEM data from the Scarborough gas field using a transdimensional 2-D parametrization. Geophys. J. Int. 199 (3), 1847–1860. https://doi.org/10.1093/gji/ggu370.

Revil, A., Florsch, N., Mao, D., 2015. Induced polarization response of porous media with metallic particles – part 1: a theory for disseminated semiconductors. Geophysics 80 (5), D525–D538. https://doi.org/10.1190/geo2014-0577.1.
Revil, A., Mao, D., Shao, Z., Sleevi, M.F., Wang, D., 2017. Induced polarization response of porous media with metallic particles – part 6: the case of metals and semimetals. Geophysics 82 (2), E97–E110. https://doi.org/10.1190/geo2016-0389.1.
Revil, A., Vaudelet, P., Su, Z., Chen, R., 2022. Induced polarization as a tool to assess mineral deposits: a review. Minerals 12 (5), 571. https://doi.org/10.3390/min12050571.
Römer, A., 2024. Projekt ÜLG83/POTGRAF, Potenzialabschätzung ausgewählter Grafitvorkommen/−lagerstätten in der Böhmischen Masse, Jahresbericht 2023.
Römer, A., Schedl, A., Ottowitz, D., Benold, C., 2021. A geophysical/geochemical exploration strategy for graphite applied in an abandoned graphite mine in Lower Austria. BHM Berg-und Hüttenmännische Monatshefte 166, 193–200. https://doi.org/10.1007/s00501-021-01097-z.
Römer, A., Ottowitz, D., Preiner, A., Benold, C., Schuberth-Hlavac, G., Auer, C., Träxler, B., Knoll, T., 2022. Potenzialabschätzung ausgewählter Grafitvorkommen/−lagerstätten in der Böhmischen Masse: Jahresbericht 2021. - 42, 25 Abb., 1 Tab., Wien.
Sakita, A.M., Della Noce, R., Gastelois, P.L., Macedo, W.A., Lavall, R.L., 2022. Binder-free graphitic films with high conductivity for supercapacitor devices. Chem. Eng. J. 427, 131731. https://doi.org/10.1016/j.cej.2021.131731.
Sambridge, M., Mosegaard, K., 2002. Monte Carlo methods in geophysical inverse problems. Rev. Geophys. 40 (3), 1–3. https://doi.org/10.1029/2000RG000089.
Sandersen, P.B.E., Kallesøe, A.J., Møller, I., Høyer, A.S., Jørgensen, F., Pedersen, J.B., Christiansen, A.V., 2021. Utilizing the towed transient electromagnetic method (tTEM) for achieving unprecedented near-surface detail in geological mapping. Eng. Geol. 288, 106125. https://doi.org/10.1016/j.enggeo.2021.106125.
Schuster, R., Pestal, G., Reitner, J., 2006. Erläuterungen zur Geologischen Karte der Republik Österreich 1: 50.000 Blatt 182 Spittal an der Drau.
Seigel, H.O., Vanhala, H., Sheard, S.N., 1997. Some case histories of source discrimination using time-domain spectral IP. Geophysics 62 (5), 1394–1408. https://doi.org/10.1190/1.1444244.
Sharifi, F., Tezkan, B., Ibraheem, I.M., Bergers, R., Yogeshwar, P., 2024. Recovering induced polarization effects from 1-D coupled inversion of transient electromagnetic data. Geophys. J. Int. 238 (3), 1708–1722. https://doi.org/10.1093/gji/ggae237.
Simandl, G.J., Paradis, S., Akam, C., 2015. Graphite deposit types, their origin, and economic significance. In: British Columbia Ministry of Energy and Mines & British Columbia Geological Survey, 3, pp. 163–171.
Spies, B.R., 1989. Depth of investigation in electromagnetic sounding methods. Geophysics 54 (7), 872–888. https://doi.org/10.1190/1.1442716.
Tian, H., Graczyk-Zajac, M., Kessler, A., Weidenkaff, A., Riedel, R., 2024. Recycling and reusing of graphite from retired lithium-ion batteries: a review. Adv. Mater. 36 (13), 2308494. https://doi.org/10.1002/adma.202308494.
Ucik, F.H., 1992. Graphit in Kärnten.
Weber, L., Schedl, A., Lipiarski, P., 2019. IRIS online (interactive raw materials information system), an example for a worldwide unique raw materials information system. BHM Berg-und Hüttenmännische Monatshefte 164, 56–66. https://doi.org/10.1007/s00501-018-0810-0.
Wong, J., 1979. An electrochemical model of the induced-polarization phenomenon in disseminated sulfide ores. Geophysics 44 (7), 1245–1265. https://doi.org/10.1190/1.1441005.
Wu, Y., Peruzzo, L., 2020. Effects of salinity and pH on the spectral induced polarization signals of graphite particles. Geophys. J. Int. 221 (3), 1532–1541. https://doi.org/10.1093/gji/ggaa087.
Wu, X., Xue, G., Fang, G., Li, X., Ji, Y., 2019. The development and applications of the semi-airborne electromagnetic system in China. Ieee Access 7, 104956–104966. https://doi.org/10.1109/ACCESS.2019.2930961.
Yogeshwar, P., Küpper, M., Tezkan, B., Rath, V., Kiyan, D., Byrdina, S., Cruz, J., Andrade, C., Viveiros, F., 2020. Innovative boat-towed transient electromagnetics – investigation of the Furnas volcanic lake hydrothermal system, Azores. Geophysics 85 (2), E41–E56. https://doi.org/10.1190/geo2019-0292.1.
Yu, C.T., Liu, H.F., Zhang, X.J., Yang, D.Y., Li, Z.H., 2013. The analysis on IP signals in TEM response based on SVD. Appl. Geophys. 10 (1), 79–87. https://doi.org/10.1007/s11770-013-0366-4.
Zeng, S., Hu, X., Li, J., Farquharson, C.G., Wood, P.C., Lu, X., Peng, R., 2019. Effects of full transmitting-current waveforms on transient electromagnetics: insights from modeling the Albany graphite deposit. Geophysics 84 (4), E255–E268. https://doi.org/10.1190/geo2018-0573.1.
Zhdanov, M.S., 2002. Geophysical Inverse Theory and Regularization Problems, vol. 36. Elsevier.
Zhu, Z., Shan, Z., Pang, Y., Wang, W., Chen, M., Li, G., Sun, H., Revil, A., 2024. The transient electromagnetic (TEM) method reveals the role of tectonic faults in seawater intrusion at Zhoushan islands (Hangzhou Bay, China). Eng. Geol. 330, 107425. https://doi.org/10.1016/j.enggeo.2024.107425.